Annex 3

Production of emulsions in shear flow
experimental and numerical study

Break-up of liquid jet in co-flow
experimental study

Institute of Fundamental Technological Research
Polish Academy of Sciences
Swietokrzyska 21, 00-049 Warsaw, Poland

Slawomir Blonski, M.Sc. Eng.
Piotr Korczyk, M.Sc.
Prof. Tomasz A. Kowalewski, Ph.D., D.Sc.

Warsaw, December 2005

Contents:

Introduction

Two experimental cases are investigated. In the first one the breakup of oil droplets is studied in a shear flow. In the second case the capillary instability and generation of droplets is studied for liquid jet in co-flow of other immiscible liquid. The purpose of the investigations is to develop procedure for well-controlled generation of mono-dispersed suspension of micro droplets. These droplets will form a matrix for collection of nano-particles into well-structured configuration. In both experimental studies similar experimental set-up and fluids are used.

The main part of the apparatus consists of microscope, channel with transparent windows, light source and digital camera. The shear flow dispersion of oil in water is studied for single processor emulsifier constructed in the University of Sophia. The process is investigated experimentally and numerically to elucidate conditions for oil droplets break-up. The flat 2-D emulsifier is constructed to ease optical access, hence to permit application of optical methods for measuring flow velocity field (PIV method) and to visualize emulsion droplets. It is a two dimensional replica of the central cross-section of cylindrical emulsifier used in the University of Sophia. Two slightly different versions of the plain emulsifier processing part are used. The main difference is in the length of a gap (Fig. 1), being 1mm or 2mm. The 2mm long gap has transparent section made of Plexiglas to permit back light illumination that is necessary for droplet observations within the gap. The following results are given for the geometry with 1mm long gap (G1) and with 2mm long gap (G2).

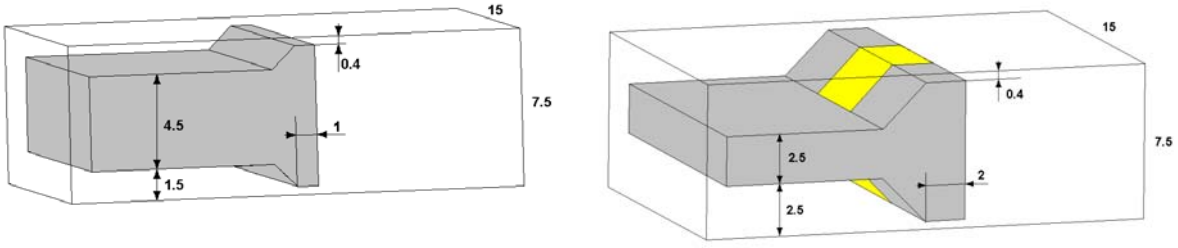

(a) (b)

Figure 1. Geometry of the processing element for two-dimensional emulsifier; (G1) – 1mm gap length, (G2) – 2mm gap length, processing element with the transparent widow. The gap height and width are 0.4mm and 15mm, respectively.

The jet breakup is studied in the rectangular cavity with two glass windows and cylindrical inlet and outlet channels. The carrier fluid (water or water-alcohol mixture) is forced through the channel using precision stroke pump. The inlet opening is equipped with a 0.8mm syringe needle that delivers concentric oil jet into the flow system. For details see figure 2.

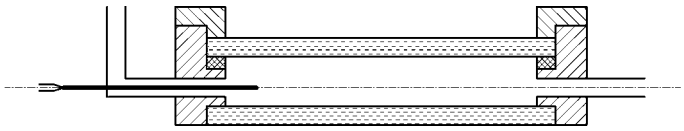

Figure 2. Scheme of the channel for jet break-up observation (geometry G3). Oil jet is issued from the needle into co-flow of water-alcohol solution. Channel length 30mm, height 8mm and width 10mm. The co-flow inlet diameter is 3mm. The needle external and internal diameter are 0.8mm and 0.5mm, respectively. The flow is illuminated through the bottom glass window and observed through the upper glass window.

The study aims to elucidate following problems:

I. Flow structure in the vicinity of the processing element. Experimental measurements of the instantaneous and average velocity fields for water flow at volumetric rates: $Q_1 = 0.13$ dm^3/s and $Q_2 = 0.204$ dm^3/s using processing element G1.

II. Visualization of droplets breakup and emulsion flow in the vicinity of the processing element for the flow rate Q_2 using processing element G2. Emulsions are prepared using 10mM NaCl solution in de-ionised water, without surfactant or with 1%wt anionic surfactant sodium dodecyl sulphate (SDS). Two different silicone oils are used to change the droplet phase viscosity: S50 (50mPas) and S500 (500mPas). The flow rate is $Q_2 = 0.204$ dm^3/s.

III. Visualization of liquid jet breakup and droplet formation for co-flow in the geometry G3. The carrier flow rates Q_e and the jet flow rate Q_j are varied flow parameters. The carrier fluid is water-alcohol solution with 1%wt anionic surfactant sodium dodecyl sulphate (SDS). Two different silicone oils are used to change the droplet phase viscosity: S50 (50mPas) and S500 (500mPas).

IV. Numerical simulation for the flow of water in the geometry G1 and G2 for the flow rate Q_2 using direct unsteady simulation and k-ε turbulence steady average flow model to reproduce flow structure and turbulence characteristics in the vicinity of the processing element.

Experimental

The experimental set-up consists of bottle with pressurized nitrogen and pressure compensation reservoir attached to the supply bottle containing working liquid. The gas pressure is stabilized at selected level using compensation reservoir. Under applied gas pressure liquid is driven through the homogeniser to the collecting bottle. The flow rate is set varying the reservoir pressure and using system of valves. The exact value of the flow rate is obtained by measuring time necessary to fill up a calibrated quantity of the collecting bottle.
When emulsion is used, the experiment is repeated several times by pouring liquid from the collecting bottle back to the supply bottle using a by-pass tube. The experiment with the emulsion starts after "manual-shaking" of water-oil mixture prepared in the supply bottle. Usually 5 to 10 passes are used to record development of the emulsion in the vicinity of the processing element.
Due to small scales of investigated objects the flow is examined by microscope. Nikon epi-fluorescence (Eclipse50i) microscope equipped with four far field lenses: 4x/NA0.13/WD17.1mm, 10x/NA0.3/WD17.30mm, 20x/NA0.35/WD24mm, and 50x/NA0.45/WD17mm is used to obtain different magnification ratios. Flow observed under the microscope reveals large relative displacements. Application of high-speed recording techniques is essential. At the highest magnification ratio the 1280 pixels image width corresponds to 0.172mm, and for the flow velocity of 1m/s the illumination time necessary to freeze images must be less than 100ns. Such short illumination time can be achieved using pulsed laser light only.
Three different light sources are used: (i) built-in microscope halogen lamp with condenser for backlight illumination; (ii) CW 5W Argon laser (496nm+515nm) for epi-fluorescence and flow visualization; (iii) Nd:YAG 30mJ (532nm) double pulsed laser used for epi-fluorescence flow velocity measurements (PIV) and as a 5ns short backlight illumination for emulsion imaging.

For the flow study two high-resolution (1280x1024pixels) 12bit cameras are used. For short exposure imaging the PCO SensiCam is used. The camera coupled with the double pulse laser permits acquisition of two images at the time interval 200ns and exposition time of 5ns. However, the pairs of images can be registered at about 3.75Hz only. For high-speed flow visualisation the second camera PCO1200hs is used. This camera permits recording full resolution images (1280x1024pixels) at 636fps, and at over 40kfps for decreased vertical image resolution. An electronic shutter of the camera allows to freeze relatively high-speed motion, however at the cost of overall light intensity. Therefore, using continuous illumination (halogen lamp, Argon laser) the shortest viable illumination time using this camera appeared to be 1ms.

Ad. I Flow structure measurements

The micro-flow measurements are based on epi-fluorescence illumination and high speed imaging, allows to collect detailed data on turbulent shear stresses in the flow, necessary for modelling the emulsification process. The flow structure study is based on micro-PIV technique, permits measurements of instantaneous two-dimensional velocity fields for selected sections of the channel. The experimental set-up consists of the experimental emulsifier cell, epi-fluorescence microscope, high resolution PIV camera, double pulse Nd:YAG laser (5ns pulse) and pressure system for flow acceleration. Flow structure is measured in a simple model of shear flow induced emulsifier. It consists of a small channel formed between two glass plates separated by a triangular obstacle (Fig. 1). Water is pumped under pressure through a small slit between the obstacle and sidewalls of the channel. Observations of the flow are performed through a transparent top or bottom wall. Flow in the vicinity of the channel centre defined by the vertical symmetry plane is analysed.
The PIV velocity measurements are performed using seeding of fluorescent polystyrene spheres, 2μm in diameter (Duke Scientific Inc.). The particle density is very low (<0.0001%wt), hence they do not affect the flow structure. Particle Image Velocimetry (PIV) based on correlation of pairs of images is used to evaluate instantaneous velocity field in the channel. These full field data allow evaluation of local velocity gradients, hence for estimation of conditions for the droplet break-up.
Unlike typical PIV methods, micro-PIV does not utilize a thin laser sheet to illuminate the seeding particles. The whole investigated volume is flooded with the laser light using beam expander and the microscope objective (Fig. 3), instead. Once the particles are exposed to the 532nm (green) light from the laser, they emit red light with an emission maximum at 612nm, as specified by the supplier. The time-span in which particles continue to fluoresce after the laser pulse is on the order of nanoseconds, so motion induced blurring of the particles does not occur in the PIV images. Two low pass filters mounted between the objective and camera permits only the fluorescent red light to pass, while preventing the green laser light to be detected by the camera. Hence, the PIV images present well detectable bright spots of seeding particles. Only particles being within depth of focus are recorded. Particles out of focus add background noise limiting applicability of the technique to thin fluid layers (max. 10-15mm). The flow is observed through the upper window. By traversing the field of observation in the horizontal and vertical direction, the position of the interrogated flow plane is selected. The vertical resolution depends on the depth of field of the objective. In the micro-PIV experiments performed using 10x objective the vertical resolution is estimated to be 10μm. The horizontal resolution of the velocity field measurements for this objective is 0.5μm. The accuracy of the velocity measurement depends on several experimental factors (quality of images, seeding concentration, particle displacement), as well as on the vector evaluation

procedure. Using in house developed software the error of velocity measurement is estimated to be below 5%.

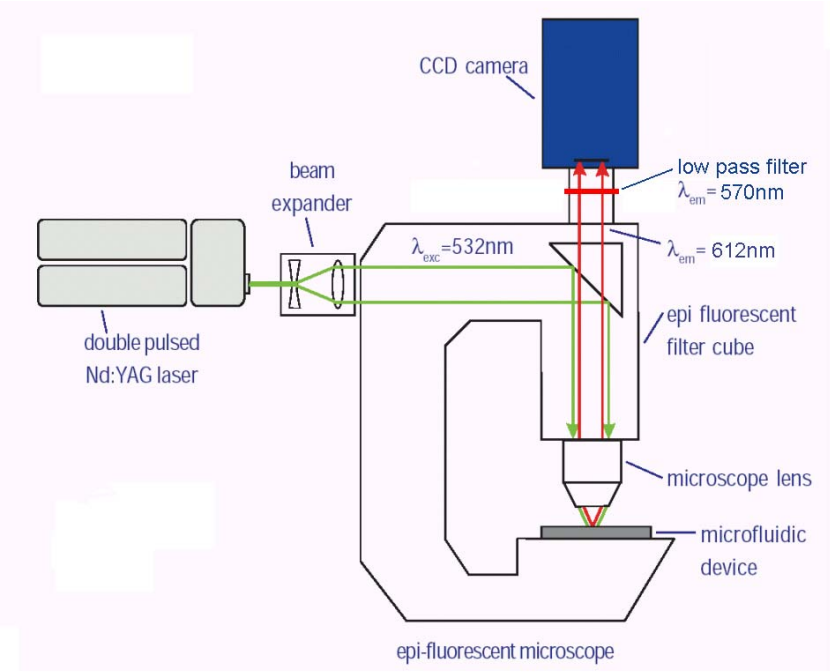

Figure 3. Scheme of the micro-PIV experimental set-up.

Ad. II Visualization of droplets breakup in emulsifier

The break-up of droplets under high-speed flow conditions is visualised using experimental set-up similar to the one described above. The set-up consists of the experimental emulsifier cell, high resolution PIV camera (PCO SensiCam), double pulse Nd:YAG laser (5ns pulse) and pressure system for flow acceleration. To visualize droplets shape in emulsion passing through the channel the bright field illumination is used. The experiments of emulsion visualisation are performed in the geometry G2, with a small (4mm) Plexiglas window implemented in the centre part of the processing element (Fig. 1b). It allows backlight illumination of the gap region. The illumination system uses laser light reflected by a diffuser. The laser light pulses passes through the backlight illumination system of the microscope with a built-in condenser. After passing the investigated channel the laser light is guided through the microscope objective to the camera. The system is used to record pairs of images at time intervals from 200ns to 1ms at 3.5Hz repetition rate. The illumination time of 5ns is set by the laser pulse duration. It allows to obtain sharp images of droplets at the highest flow rates used in the study. However, due to the coherent structure of the laser light unavoidable speckle overlay is present in the images. Most of the experiments with emulsion are carried out at flow rate $Q = 0.204$ dm^3/s and several series of experiments are performed at lower flow rate, $Q = 0.13$ dm^3/s, to study the effect of the Reynolds number on the drop break-up.

Ad. III Visualization of liquid jet instability and droplet formation in co-flow

The liquid jet break-up is commonly used method for dispersing liquids jets in air. The present study is intended to obtain dispersions of small droplets in other liquid. In the

experimental set-up, the jet is issued from the 0.8mm needle (0.5mm internal diameter) inserted into the channel described above as geometry G3. The images of the jet are recorded by a high-speed camera (PCO 1200hs) at 500 frames/s. To obtain sharp images of the jet and droplets the camera electronic shutter is set to 0.1ms. The standard halogen illumination system of the microscope is used for backlight illumination. Image processing software is used to improve the quality of the images as well as to measure dimensions.

Ad. IV Numerical simulation

Both turbulent and laminar flow models have been applied using Fluent 6.2 package. Details on the numerical procedure, investigated geometry and the description of results are given in Part 4 of the report.

Photos of the experimental set-up

Figure 4. Experimental set-up for micro PIV technique measurements and drops break-up process investigation: Nikon Eclipse50i microscope, PCO1200hs high-speed camera (for drops observation; for PIV measurements are used other camera: PCO SensiCam), pressure system for flow acceleration and PC computer for data acquisition.

Figure 5. Experimental set-up for investigation of jet break-up process; pressure system is replaced with two precision syringe pumps.

Figure 6. Emulsifier model installed under microscope.

Figure 7. Transparent processing element.

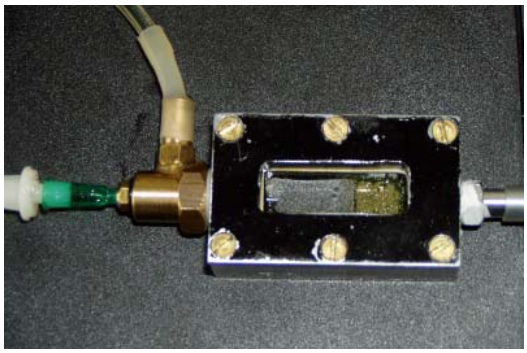

Figure 8. Experimental chamber for investigation of break-up process of liquid jet in co-flow.

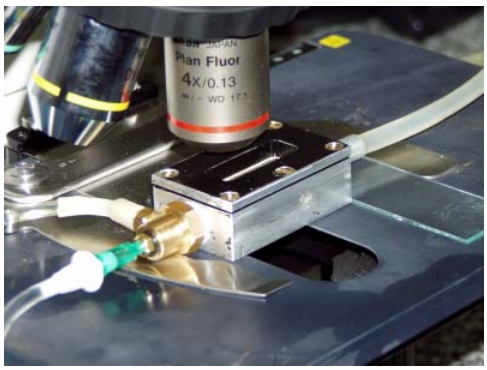

Figure 9. Experimental chamber for investigation of break-up process of liquid jet in co-flow installed under microscope.

1. Flow structure investigation in the vicinity of the processing element by Particle Image Velocimetry (PIV)

1.1 Experimental set-up

All measurements in this part were taken for geometry G1 (length of gap 1mm), and flow rate $Q_2 = 0.204$ dm^3/s.
PIV technique allows measurements of velocity field by use of optical non-intrusive methods. In the case of this experiment pairs of microscopic images of flow were collected and than processed to retrieve field of velocity on the plane of image. Images were taken in the horizontal plane, so only horizontal components of velocity field could be obtained without any information about vertical component.
Figure 1.1 shows geometry of the experimental domain. Axes *x* and *z* are on horizontal plane and axis *y* is on vertical plane. Axis *x* starts at the end of processing element, axis *y* at the interface between glass window and interior of emulsifier. Axis *z* starts at the centre of the emulsifier.
Five profiles of velocities were obtained from the PIV measurements - each of them in different locations (Fig. 1.1 and Table 1.1).

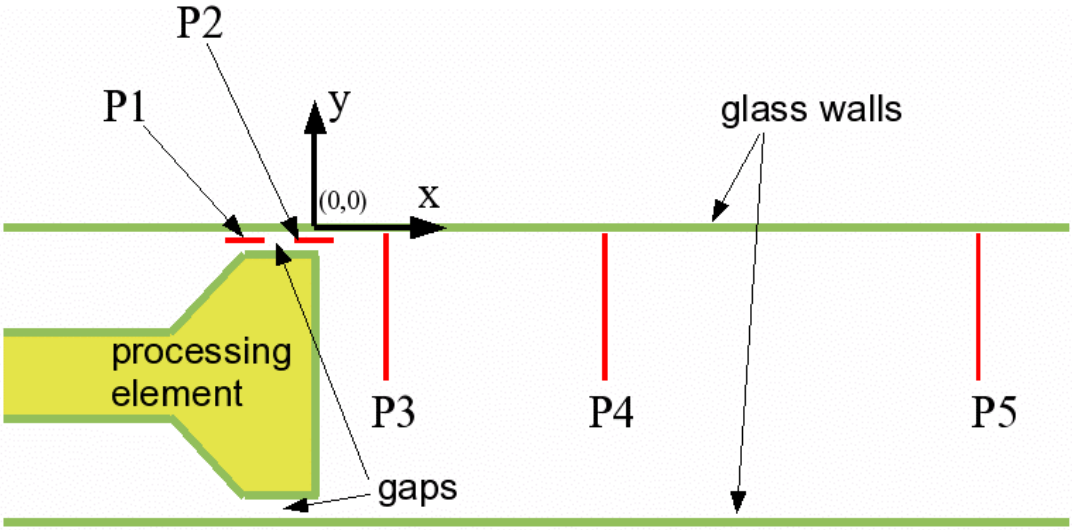

Figure 1.1 Schematic view of the emulsifier with coordinates system and positions of profiles P (*z* component is orthogonal to the plane of image). Note that point (0,0,0) is placed at the end of processing element for *x* direction, the interface glass/fluid for *y* direction, centre of the emulsifier for *z* direction.

Profile	***X [mm]***	***Y [mm]***	***Z [mm]***
P1	–1.45 ÷ –0.7	–0.2	0
P2	–0.35 ÷ 0.35	–0.2	0
P3	1	0 ÷ –3.75	0
P4	3	0 ÷ –3.75	0
P5	8	0 ÷ –3.75	0

Table 1.1. Positions of measurements for profiles.

1.2 Horizontal profiles P1 and P2

In the case of profile P1, images were centred nearly position x=-0.5mm, y=-0.2mm, z=0, what corresponds to the entrance to the gap, 0.2mm below glass window.

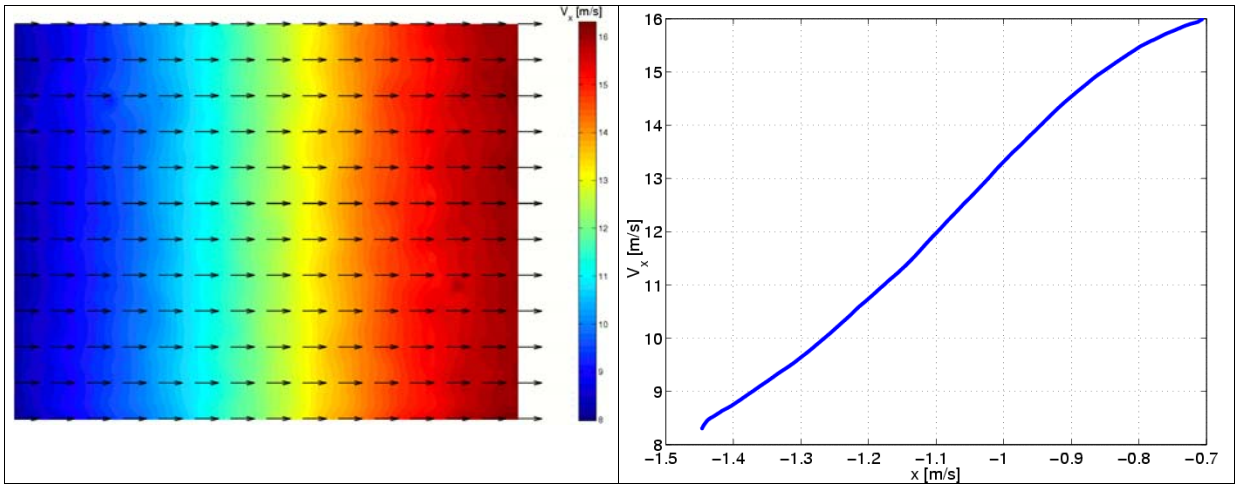

Figure 1.2. Profile P1. Left: velocity field (width of image corresponds to about 0.7mm). Right: V_x velocity for various x (obtained by averaging of velocity field along y axis), position x=-1 corresponds to the entrance to the gap.

In the case of profile P2, field of view was centred nearly position x=-0.0mm, y=-0.2mm, z=0, what corresponds to the end of the gap in the x-direction and 0.2mm below glass in the y-direction.

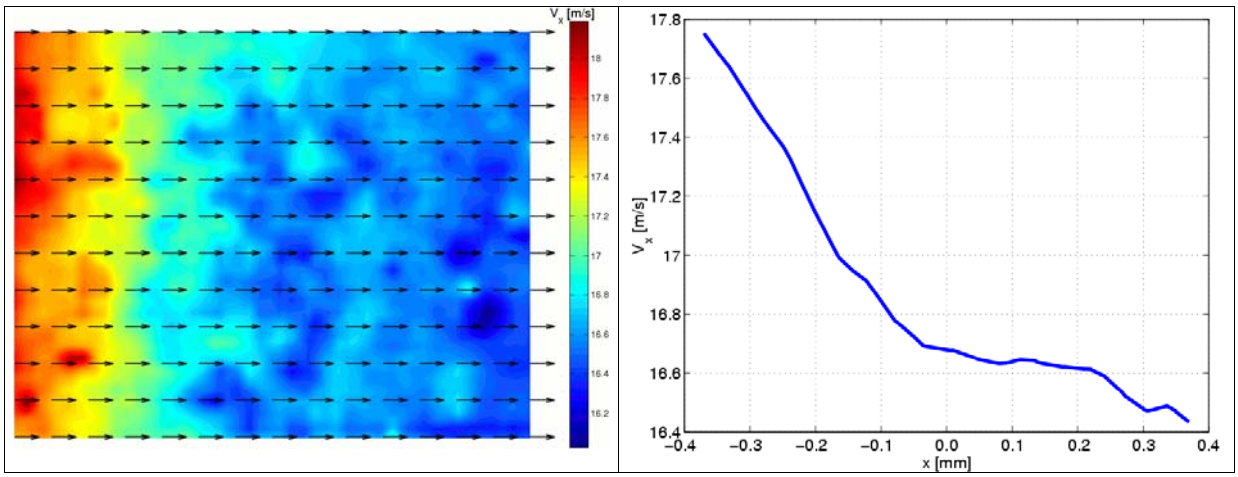

Figure 1.3. Profile P2. Left: velocity field (width of image corresponds to about 0.7mm). Right: V_x velocity for various x (obtained by averaging of velocity field along y axis), position x=0 corresponds to the end of the gap.

Value of the V_x component of velocity rises before the gap (Fig. 1.2) and decreases behind the processing element of emulsifier (Fig. 1.3).
For profiles P1 and P2 measurements of velocity field were repeated several hundred times. Any fluctuations of the velocity field in time were not observed. Flow seems to be steady.

1.3 Flow behind the processing element

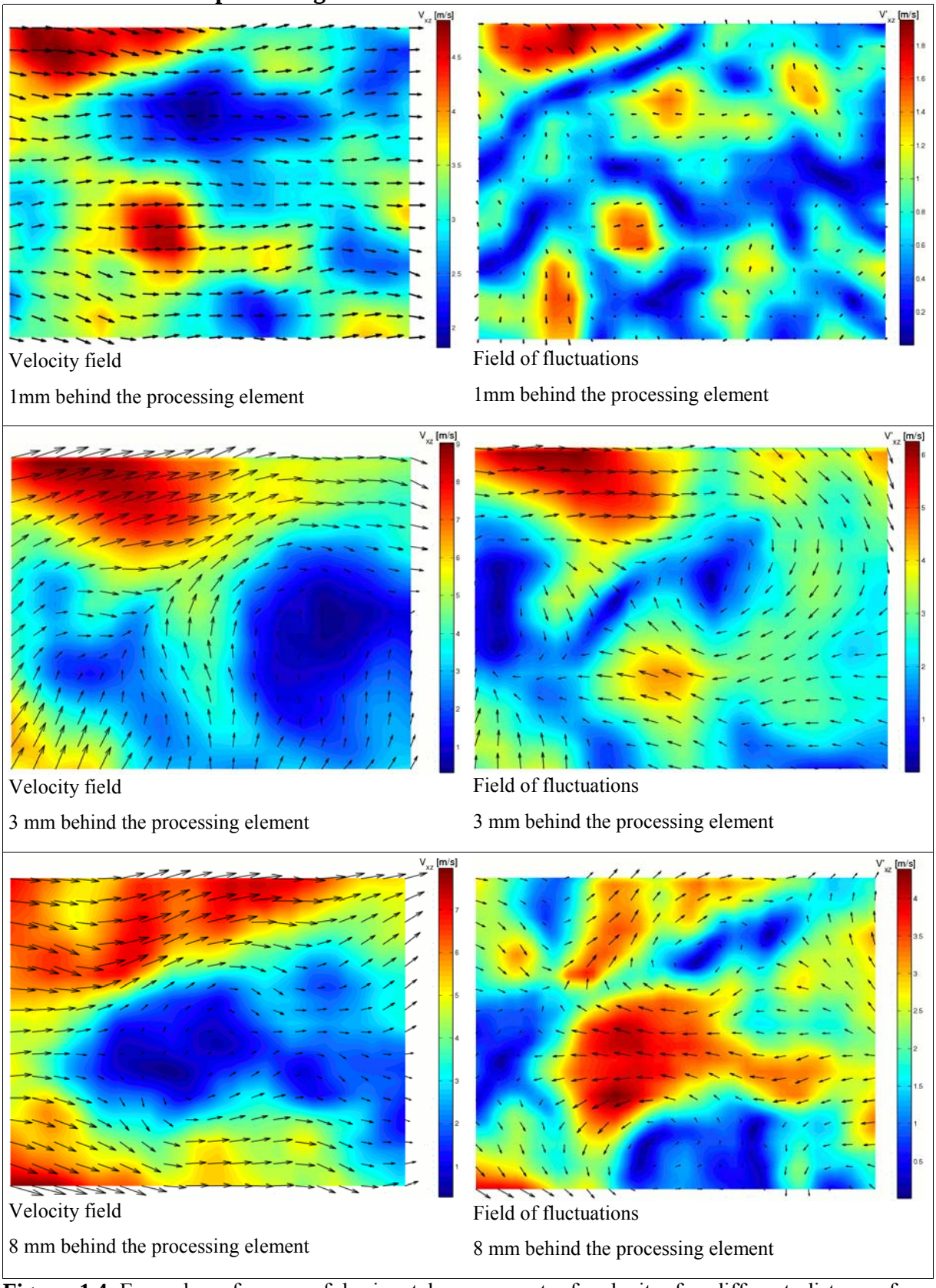

Figure 1.4 Examples of maps of horizontal component of velocity for different distance from processing element (x=1mm, x=3mm, x=8mm). For each of velocity map the field of fluctuations of velocity is shown on the right side. Magnitude of vectors is visualized by colour scale (colour bars). Width of image is about 0.7 mm in real space. The measurements were taken for y=-0.3mm (0.3mm below glass window).

Time-fluctuations of velocity appear behind processing element. Figure 1.4 shows examples of velocity field for three different x positions (x=1mm, x=3mm, x=8mm) and the same y position (y=-0.3mm). Flow consists of vortices and shear regions – structures characteristic for turbulence.

1.4 Profiles P3, P4, P5

For three positions behind processing element (P3 - 1mm, P4 - 3mm, P5 - 8mm) profiles of horizontal velocity components (V_x, V_z) along the vertical direction (y axis) were calculated. Level in y direction was set by changing distance between emulsifier and microscopic lens. Position in y was changed from y=0 (surface of glass) to y=-3.75 (centre of emulsifier).
On the each level the mean value of velocity was calculated by averaging in time. $<V_x>$ is the mean velocity for V_x, and $<V_z>$ for V_z. The fluctuations V'_x and V'_z are obtained from relations:
$V_x=<V_x>+V'_x$
$V_z=<V_z>+V'_z$
Figure 1.5 shows relations between $<Vx>$ and y for profiles P3, P4 and P5. Also relation between tke_{xz} in function of y is shown.
$tke_{xz}=<V'^2_x>+<V'^2_z>$ it is the part of TKE (mean turbulent kinetic energy), calculated from horizontal components of velocities, where $TKE=0.5(<V'^2_x>+<V'^2_z>+<V'^2_y>)$.

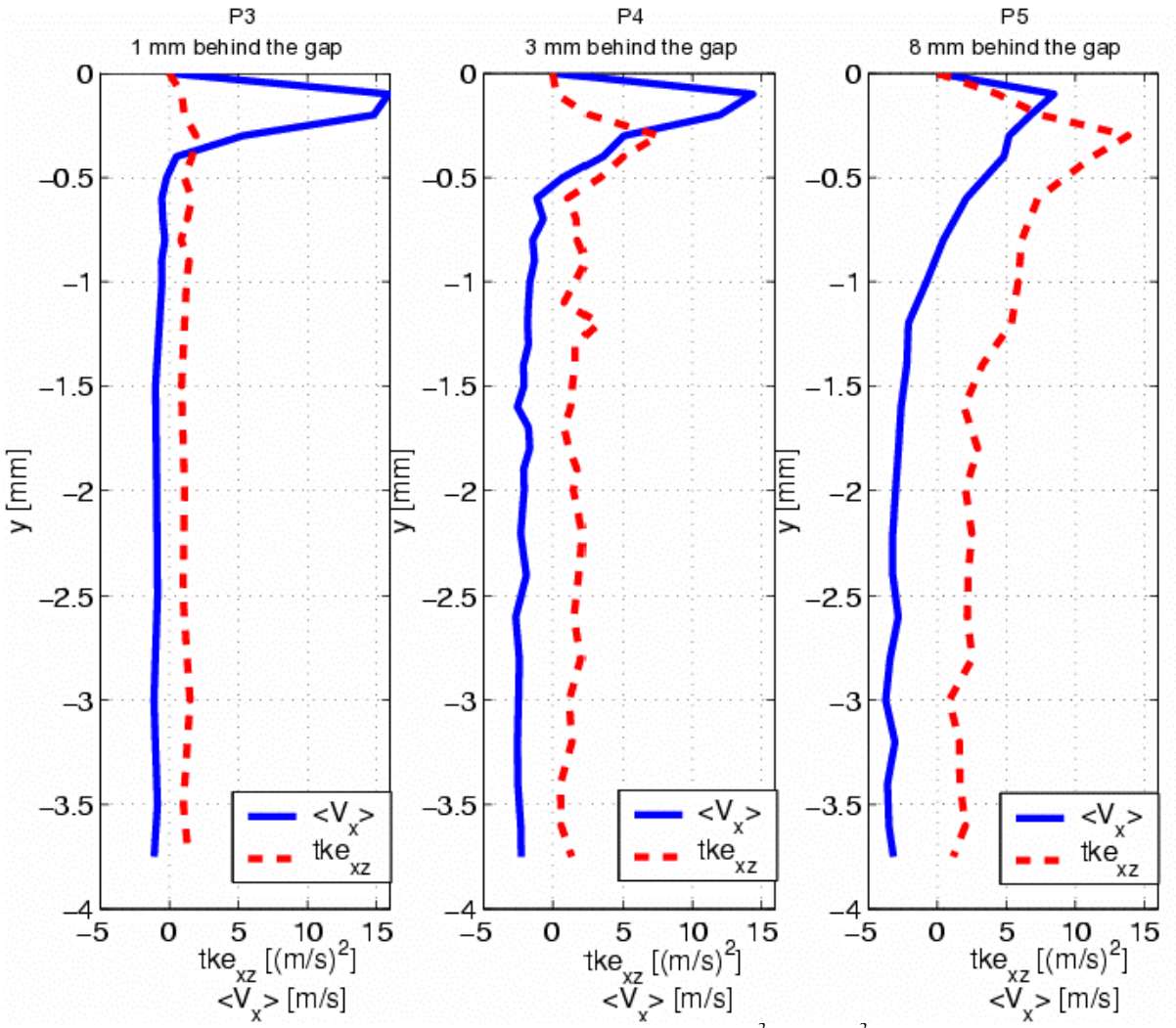

Figure 1.5 Profiles P3, P4, P5. $<V_x>$ for various y and $tke_{xz}=<V'^2_x>+<V'^2_z>$ as a function of y.

Profiles of tke_{xz} implie that turbulence appears behind the gap and develop along x direction.

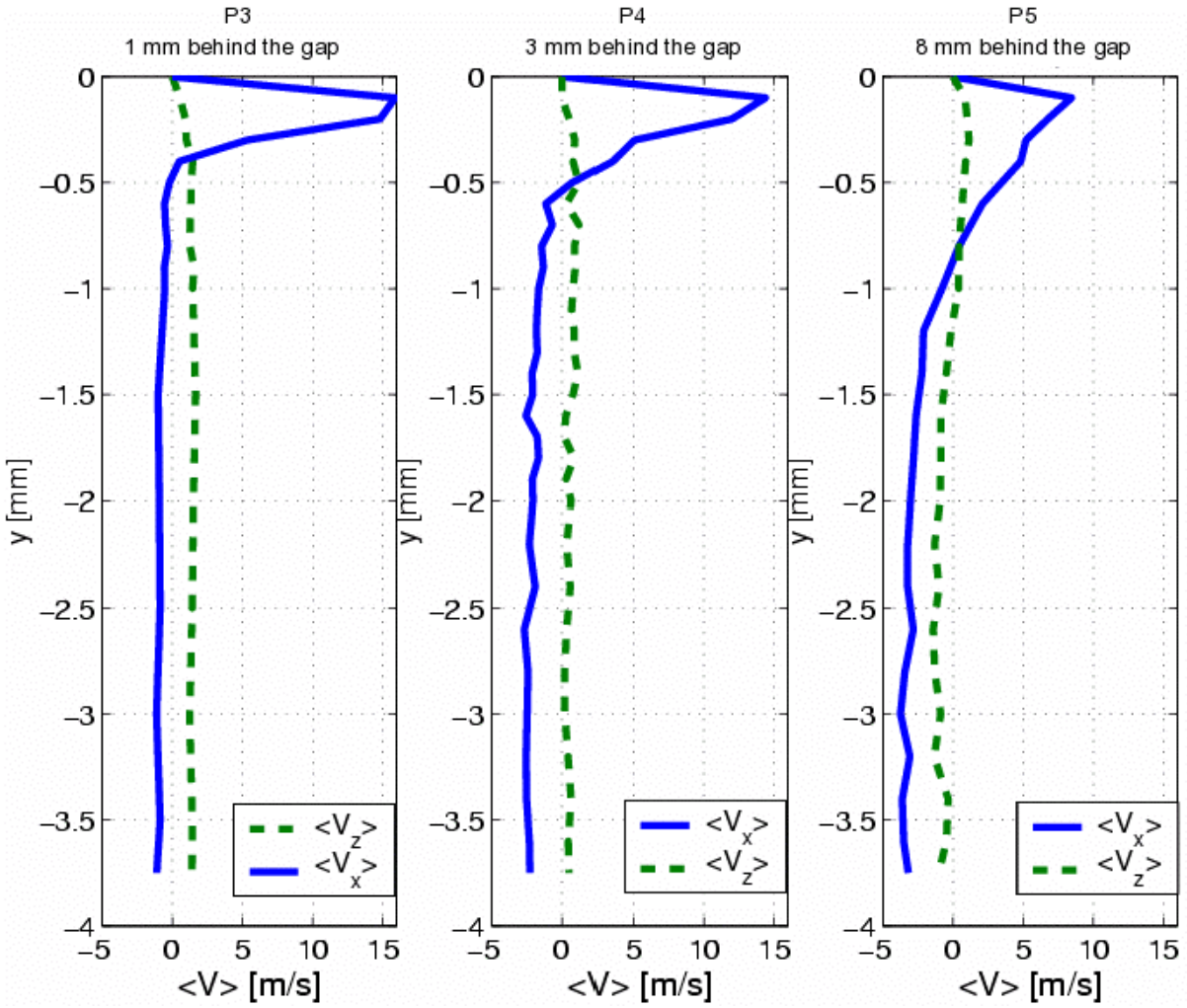

Figure 1.6 Profiles P3, P4, P5. $<V_x>$ and $<V_z>$ for various y.

Profiles of $<V_x>$ and $<V_z>$ along y show that the vector of horizontal components of velocities changes direction along y and forms spiral structures, but it should be noticed that vectors of velocities retrieved from PIV measurements consist of only two components of velocities. They are projections of 3D vectors on the horizontal plane, so real vectors may form different shapes.
Appearance of $<V_z>$ shows that probably measurements were taken not exactly at the centre of the emulsifier (not for z=0).

1.5 Structure functions for the turbulent flow behind the gap

For turbulent flow behind processing element the structure functions was calculated.
The second order transverse structure function is a mean square increment of velocity component perpendicular to the line of separation $\boldsymbol{l}$. For V_x and V_z it is defined as:

$$S_X^{\perp}(l) = < [V_X(x,z+l) - V_X(x,z)]^2 >$$

$$S_Z^{\perp}(l) = < [V_z(x+l,z) - V_z(x,z)]^2 >$$

The second order longitudinal structure function is a mean square increment of velocity between two points separated by l, projected onto the line of separation. For V_x and V_z it is defined as:

$$S_x^{\parallel}(l) = < [V_x(x+l,z) - V_x(x,z)]^2 >$$

$$S_z^{\parallel}(l) = < [V_z(x,z+l) - V_z(x,z)]^2 >$$

In case of this experiment the assumption of homogeneity of velocity field on small area of PIV measurement was used. For certain separation l, mean square increments were averaged over whole velocity field obtained from PIV measurements. In this way the curve dependent on separation l was retrieved. Than each curve obtained from different PIV measurements for the same profile and the same level y was averaged.

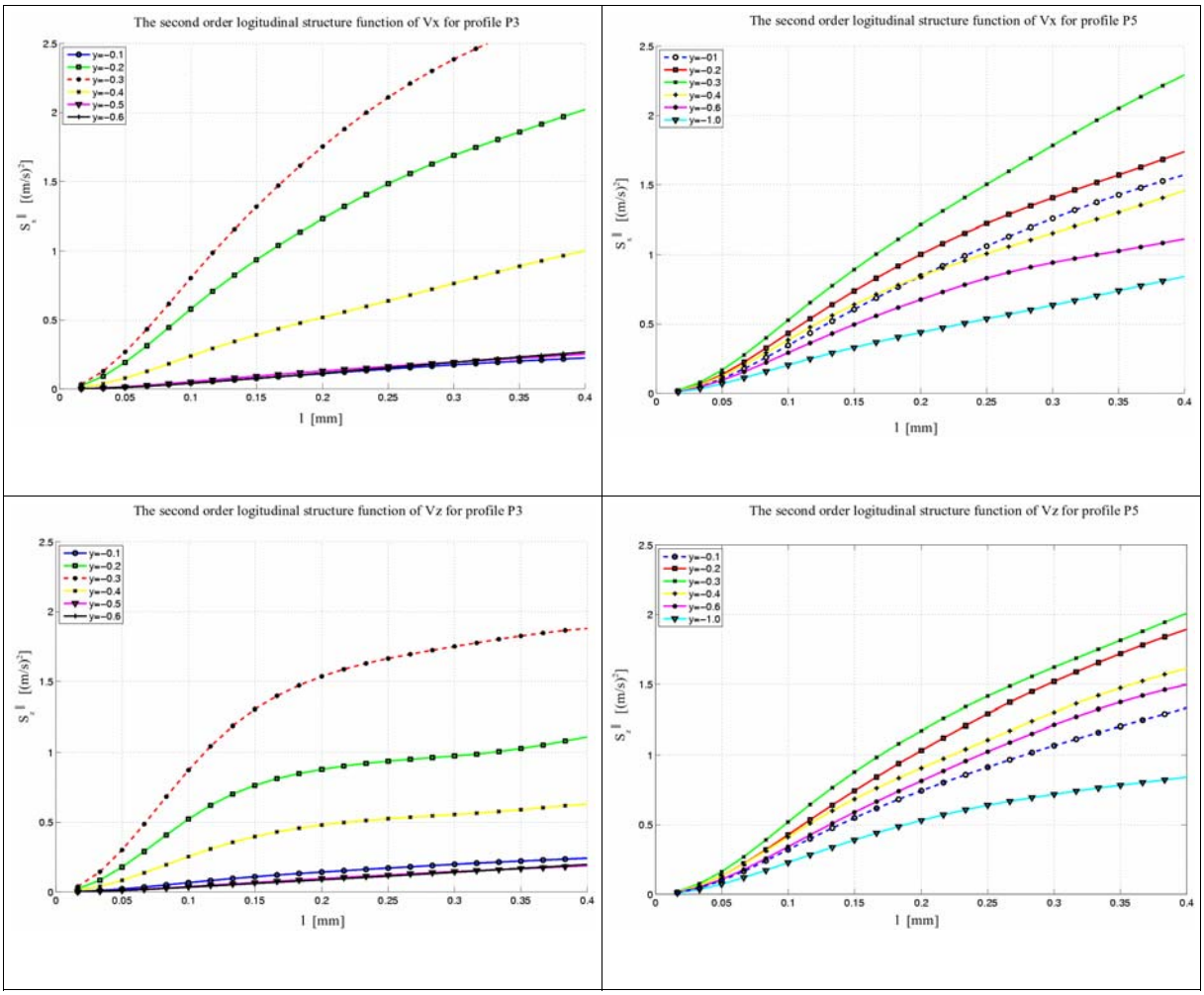

Figure 1.7 The second order longitudinal structure functions for different level y. Left – profile P3, right – profile P5. Top – structure functions for *Vx*, bottom – for *Vz*.

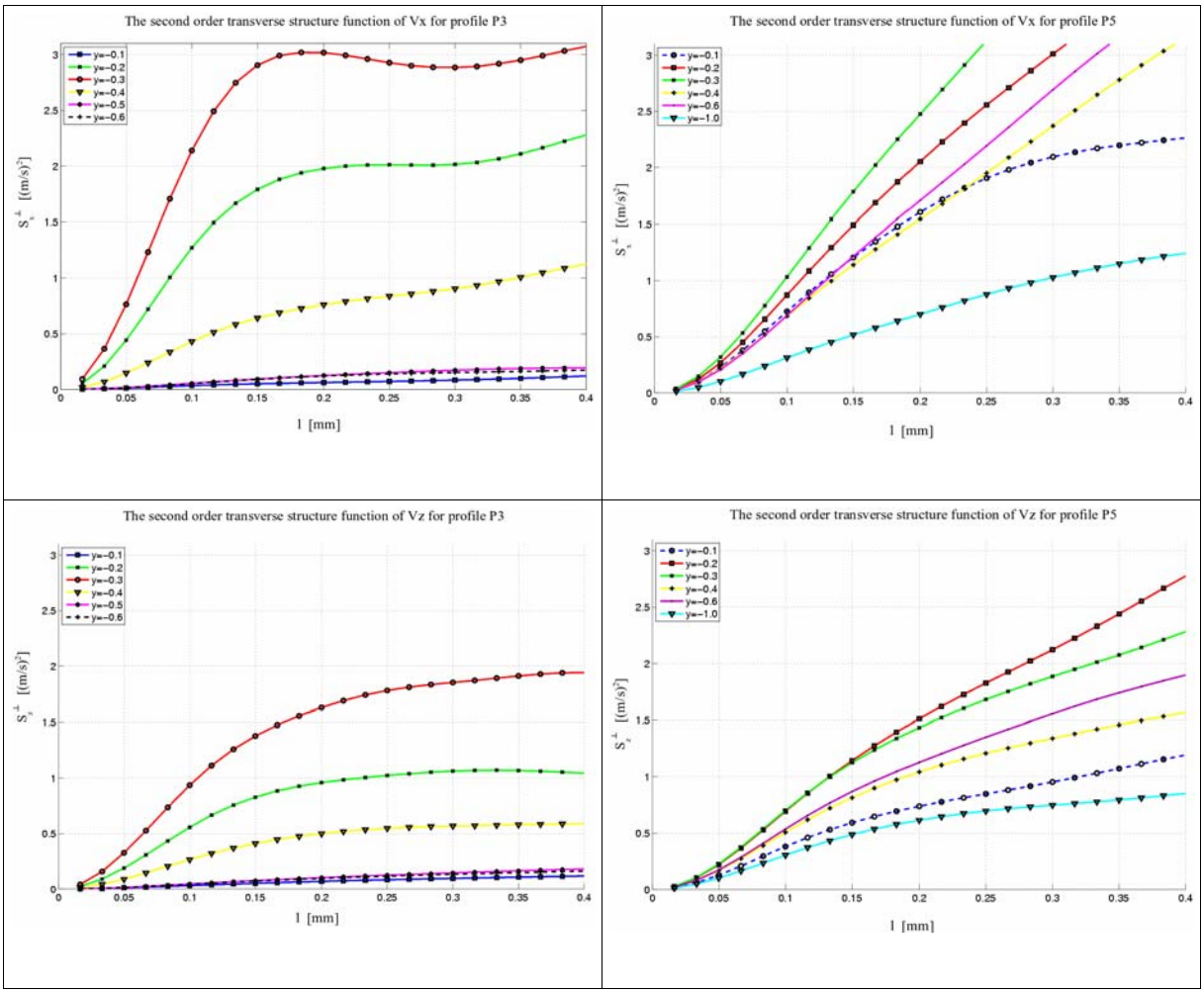

Figure 1.8 The second order transversal structure functions for different level y. Left – profile P3, right – profile P5. Top – structure functions for *Vx*, bottom – for *Vz*.

All graphs on figure 1.7 and 1.8 show that increments of V_x are larger than of V_z. The turbulent structures are anisotropic.
It can be seen that for profile P3 values represented by few curves are higher than the others. It can be deduced that for profile P3 (1mm behind the gap) on level y=-0.3 mm (0.3 mm below the glass window) the differences are largest and the region of high increments of velocity is between levels y=-0.1mm and y=-0.5mm.
For the profile P5 (8 mm behind the gap) the maximum of velocity increments is also about y=-0.3mm but range of levels of high velocity gradients is much larger than in the case of profile P3. Hence there is a trail of high velocity differences that is thin near the end of the gap and when moves along x direction get wider.
Let focus on the relation between value of structure functions and separation l. Top left graph on the figure 1.8 shows transversal structure functions of V_x for profile P3. On the level y=-0.3mm (red curve) one can observe fast rising of the curve for small l but for l>0.15 mm curve seems to be stable. Similar behaviour is observed for structure function of V_z Transversal fluctuations of velocities can be identified with vortices so it can be deduced that near the end of the gap the dominant structures of field of velocity are small strong vortices. For the profile P5 it can be shown that there are large eddies which size overdraw a range of the graph (are larger than 0.4mm).

1.6 Conclusions

The turbulence appears and develops behind the gap. There is a trail of high velocity gradients that starts near the end of the gap, moves along *x* axis and spreads in vertical direction. The maximum of velocity gradients is located about 0.3mm below the glass window. The character of turbulent velocity field changes along *x* axis. Near the end of the gap dominant structures are small vortices. Along *x* axis larger eddies develop. It suggests that small droplets <0.15 mm are more unstable 1mm behind the gap than 8mm behind processing element. On the other hand droplets >> 0.15 mm are less stable far from the gap than in the vicinity of the end of processing element.

2. Visualization of droplets breakup process and emulsion flow in the vicinity of the processing element.

2.1 Introduction – experimental set-up and used materials

Visualization of droplets breakup process was done using planar model of the emulsifier – geometry G2 (Fig. 2.1a) with transparent processing element (Fig. 2.1b) that permits optical access to the gaps between processing element and glass window.

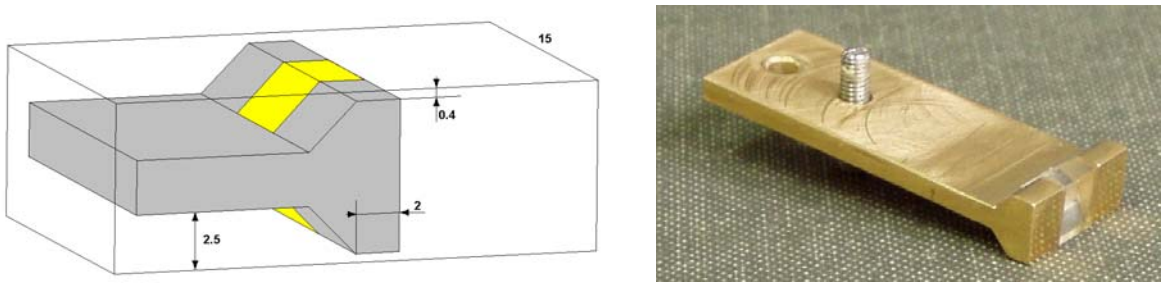

(a) (b)

Figure 2.1. Geometry of the processing element for planar emulsifier: schematic draft (a) and real photo of the transparent processing element (b).

Emulsion was prepared with 10mM NaCl solution in de-ionised water, without surfactant or with 1%wt anionic surfactant sodium dodecyl sulphate (SDS). Two silicone oils were used to change the droplet phase viscosity: S50 (50mPas) and S500 (500mPas). All experiments were done with flow rate $Q_2 = 0.204\ dm^3/s$.
Experiments were done using Nikon Eclipse 50i epi-fluorescent microscope equipped with 20x/NA0.35/WD24mm lens and PCO SensiCam camera. Double pulse Nd:YAG laser (532nm, 30mJ per pulse) was used as a light source.
All presented images of the emulsion were taken under microscope and corresponds to 432μm in width. Two consecutive images of emulsion taken at time interval 1μs or 5μs (1μs – for droplets in the gap and 5μs – for other positions in the emulsifier) are used to evaluate instantaneous velocity magnitude of the droplet V_d.

2.2 Results

Figure 2.1 shows schematic view of the part of the emulsifier model in the vicinity of the processing element with defined coordinate system.

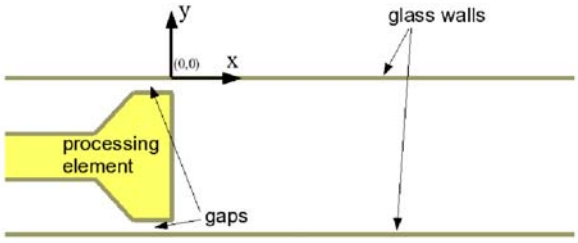

Figure 2.2. Schematic view of the emulsifier with coordinates system. Note that point (0,0) is placed at the end of processing element and the glass/fluid interface.

Table 2.1 collects list of experiments for S50 oil without surfactant and brief comments to observations.

Table 2.1. Summarized experimental results for S50 oil, emulsion without surfactant

Position in the emulsifier model	Velocity of the droplet V_d [m/s]	Comments
Gap	12.1	lack of oil-drops deformations (Fig. 2.3)
x = 0mm, y = -0.3mm (just behind processing element)	10.8	lack of oil-drops deformations (Fig. 2.4)
x = 2mm, y = -0.4mm	4.5	oil-drops deformations occurs (Fig. 2.5)
x = 5mm, y = -0.4mm	6.7	lack of oil-drops deformations (Fig. 2.6)

Figure 2.3 shows drops of S50 oil in the gap – emulsion without surfactant. No deformations of the droplets were observed.

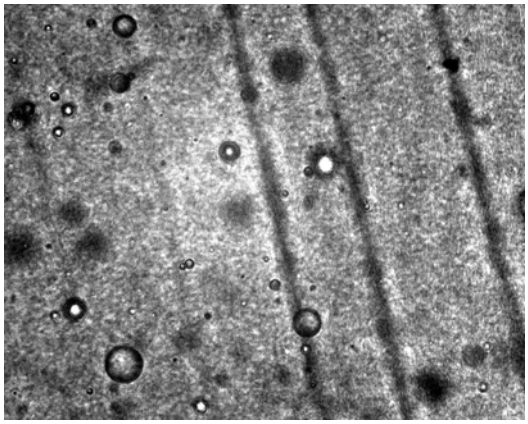

Figure 2.3. Result for S50 oil – emulsion without surfactant; oil-drops in the gap; velocity of the droplet $v_d = 12.1 m/s$; figure width corresponds to 432μm.

For the same emulsion 0.3mm below glass, just behind processing element no deformations were observed (see Fig. 2.4).

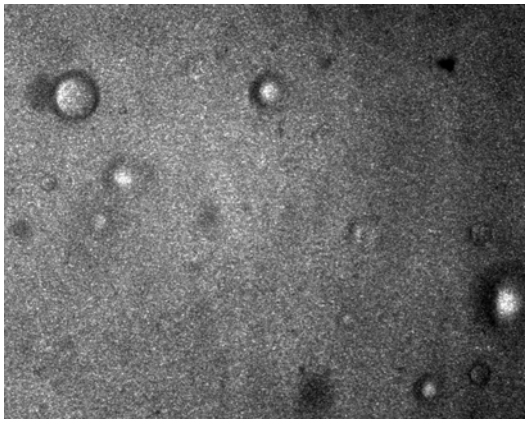

Figure 2.4. Result for S50 oil – emulsion without surfactant; oil drops just behind processing element and 0.3mm below glass wall (x = 0mm, y = -0.3mm); velocity of the droplet $v_d = 10.8 m/s$; figure width corresponds to 432μm.

Figure 2.5. shows pictures for S50 oil – emulsion without surfactant; captured 2mm behind the gap and 0.4mm below the glass wall. One can see various deformed shapes of droplets flattened by the flow. Elongated oil structures are also visible.

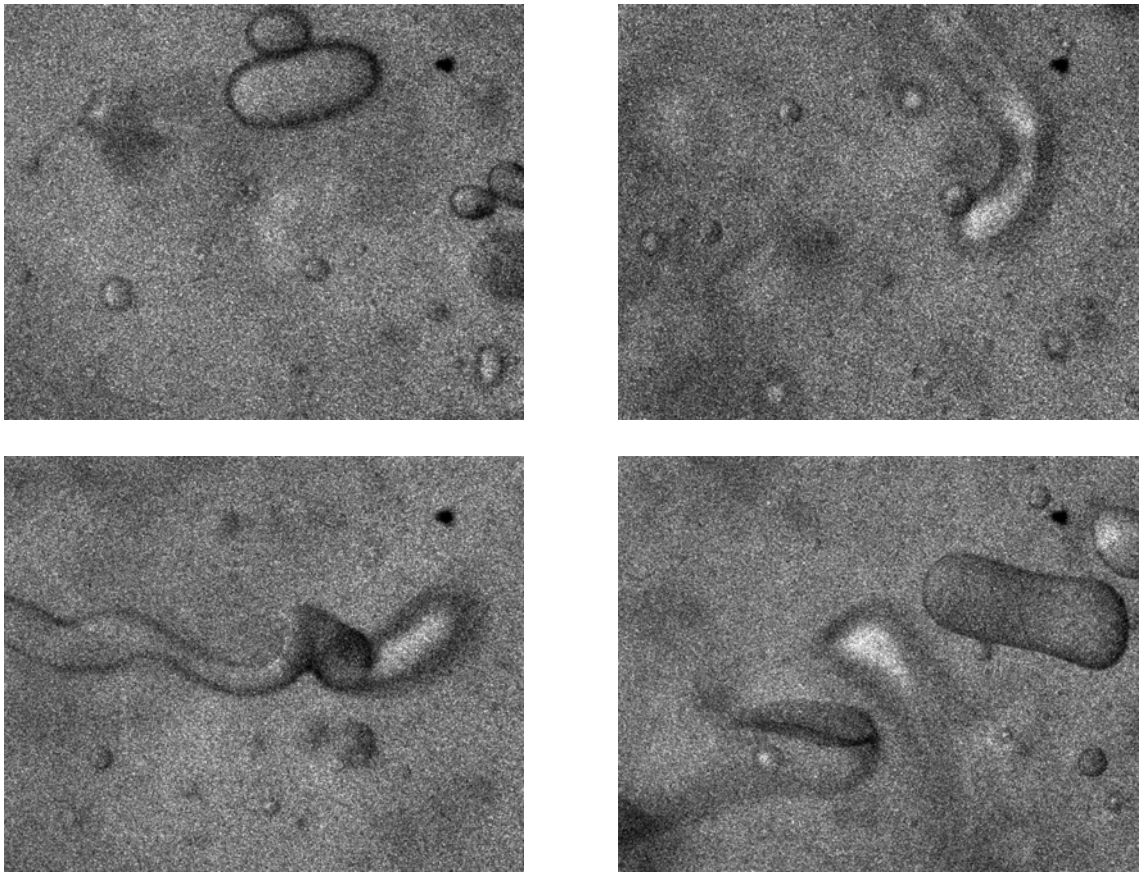

Figure 2.5. Result for S50 oil – emulsion without surfactant; oil droplets 2mm behind processing element and 0.4mm below glass wall (x = 2mm, y = -0.4mm); velocity of the droplet $v_d = 4.5 m/s$; figure width corresponds to 432μm.

Image presented in the figure 2.6 shows emulsion 5mm behind the processing element and 0.4mm below the wall. Droplets seem to be not deformed.

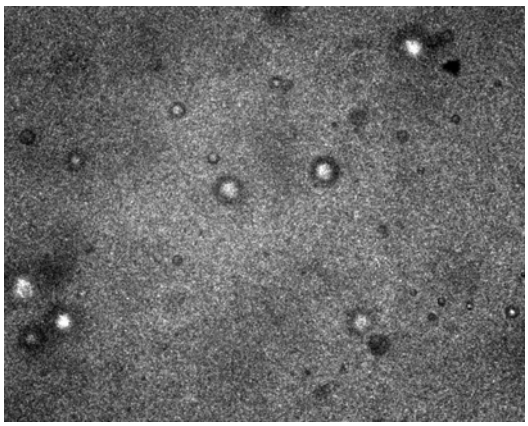

Figure 2.6. Result for S50 oil – emulsion without surfactant. Oil droplets 5mm behind processing element and 0.4mm below glass wall (x = 5, y = -0.4); velocity of the droplet $v_d = 6.7 m/s$; figure width corresponds to 432μm.

Table 2.3. Summarized experimental results for S50 oil, emulsion with 1% wt anionic surfactant sodium dodecyl sulphate (SDS).

Position in the emulsifier model	Velocity of the droplet V_d [m/s]	Comments
Gap	12.3	lack of oil-droplets deformations (Fig. 2.7)
x = 2mm, y = 0.0mm	10.3	lack of oil-droplets deformations (Fig. 2.8)
x = 2mm, y = -0.1mm	10.9	lack of oil-droplets deformations (Fig. 2.9)
x = 2mm, y = -0.2mm	9.7	oil-droplets deformations occurs (Fig. 2.10)
x = 2mm, y = -0.4mm	4.7	oil-droplets deformations occurs (Fig. 2.11)

In the figure 2.7 that visualized emulsion of S50 oil with surfactant in the gap no deformed droplets were observed.

Figure 2.7. Result for S50 oil – emulsion with 1%wt SDS surfactant; oil-droplets in the gap; velocity of the droplet $v_d = 12.3 m/s$; figure width corresponds to 432μm.

Also 2mm behind the gap on the fluid-wall interface deformations of droplets were not observed.

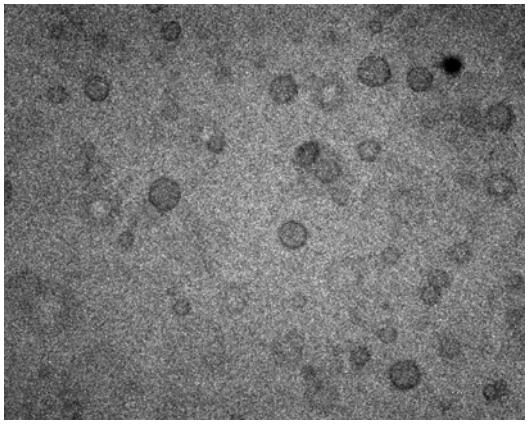

Figure 2.8. Result for S50 oil – emulsion with 1%wt SDS surfactant; oil drops 2mm behind processing element and just below glass window (x = 2mm, y = 0.0mm); velocity of the droplet $v_d = 10.3 m/s$; figure width corresponds to 432μm.

Similarly, 2mm behind the processing element, 0.1mm below glass window drops shape seems to be regular (Fig. 2.9).

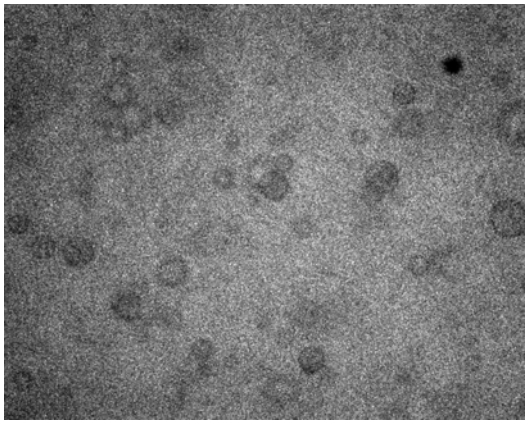

Figure 2.9. Result for S50 oil – emulsion with 1%wt SDS surfactant; oil droplets 2mm behind processing element and 0.1mm below glass wall (x = 2mm, y = -0.1mm); velocity of the droplet v_d = 10.9*m/s*; figure width corresponds to 432μm.

0.2mm below wall some deformed shapes appear (Fig. 2.10).

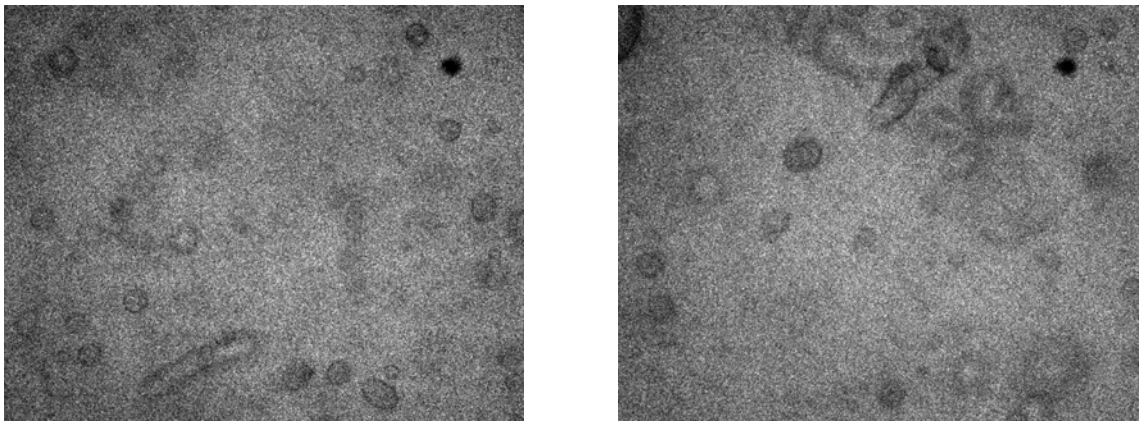

Figure 2.10. Result for S50 oil – emulsion with 1%wt SDS surfactant; oil droplets 2mm behind processing element and 0.2mm below glass wall (x = 2, y = -0.2); velocity of the droplet v_d = 9.7*m/s*; figure width corresponds to 432μm.

0.2mm deeper, in the position 2mm behind the gap and 0.4mm below wall, larger deformations were observed (Fig. 2.11).

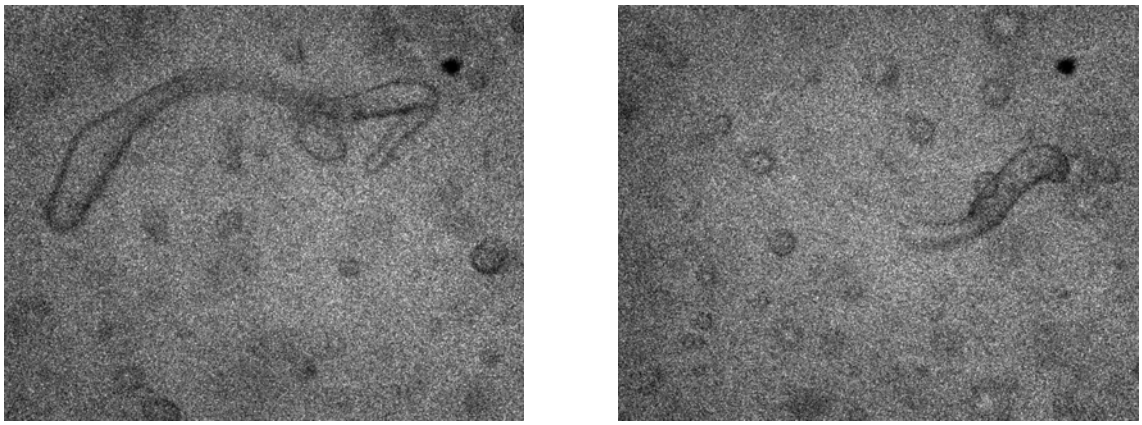

Figure 2.11. Result for S50 oil – emulsion with 1%wt SDS surfactant; oil drops 2mm behind processing element and 0.4mm below glass wall (x = 2, y = -0.4); velocity of the droplet v_d = 4.7*m/s*; figure width corresponds to 432μm.

Table 2.4. Summarized experimental results for S500 oil, emulsion with 1% wt anionic surfactant sodium dodecyl sulphate (SDS).

Position in the emulsifier model	Velocity of the droplet V_d [m/s]	Comments
Gap	12.6	lack of oil-droplets deformations (Fig. 2.12)
x = 0mm, y = -0.2mm	11.3	lack of oil-droplets deformations (Fig. 2.13)
x = 2mm, y = -0.2mm	10.5	oil-droplets deformations occurs (Fig. 2.14)

Also for oil S500 with SDS in the gap and just behind processing element no deformations were observed (Fig 2.12 and 2.13).

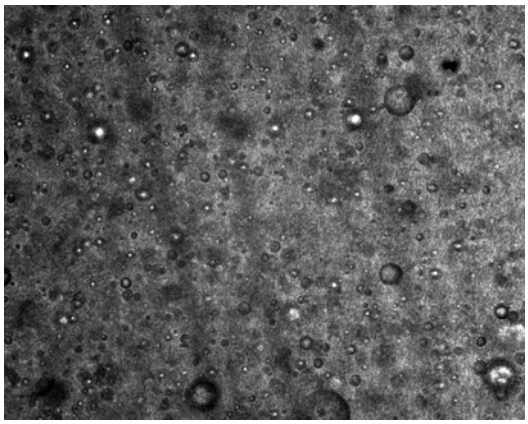

Figure 2.12. Result for S500 oil – emulsion with 1%wt SDS surfactant; oil-droplets in the gap; velocity of the droplet v_d = 12.6*m/s*; figure width corresponds to 432μm.

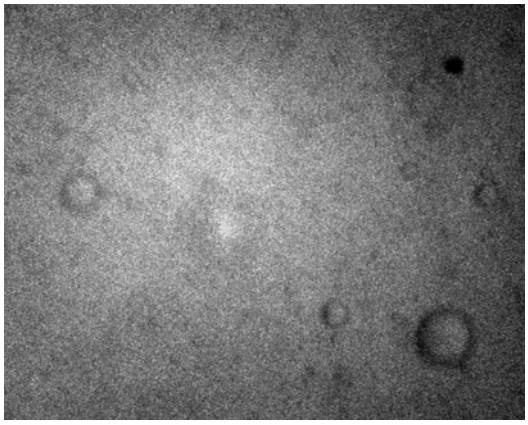

Figure 2.13. Result for S500 oil – emulsion with 1%wt SDS surfactant; oil droplets just behind processing element and 0.2mm below glass wall (x = 0mm, y = -0.2mm); velocity of the droplet v_d = 11.3*m/s*; figure width corresponds to 432μm.

Figure 2.14 shows images of deformed S500 oil droplets 2 mm behind processing element and 0.2mm below wall.

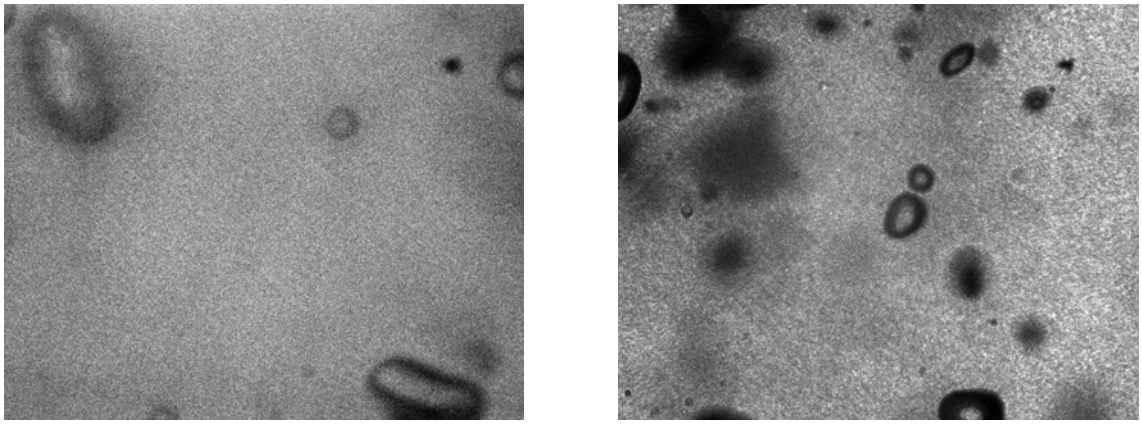

Figure 2.14. Result for S500 oil – emulsion with 1%wt SDS surfactant; oil droplets 2mm behind processing element and 0.2mm below glass wall (x = 2mm, y = -0.2mm); velocity of the droplet $v_d = 10.5 m/s$; figure width corresponds to 432μm.

Figure 2.15 shows motionless, produced emulsion created by a few dozen times passes through the emulsifier. Figure 2.15a and 2.15b present S50 and S500 oil drops, respectively, in emulsion with surfactant.

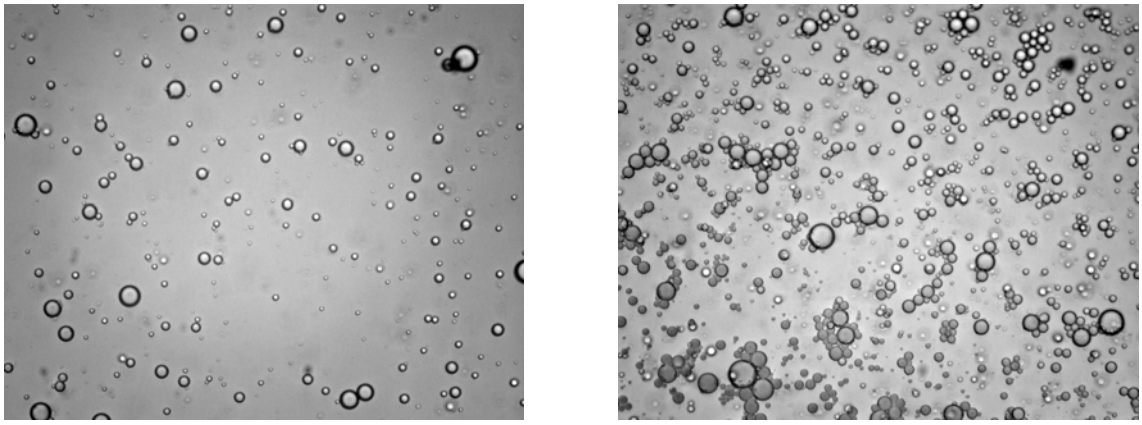

a b

Figure 2.15. Motionless emulsion observed under microscope: a) S50 oil with 1%wt SDS surfactant, b) S500 oil with 1%wt SDS surfactant; figure width corresponds to 432μm.

2.3 Conclusions

Visualisation of droplets break-up in the emulsifier indicates that the process takes place few millimetres behind processing element. “Large” droplets were not found in the gap and droplets break-up process was not observed. However, there are “large” droplets observed behind the gap. It is not clear if these droplets are created due to the agglomeration in the dead-water region (re-circulation zone after the gap), or it was not possible to find by use of experimental set-up. The flow observations were performed in the vicinity of the channel centre only. It is possible that some large droplets were trapped by the sidewalls of the gap,

not observed by camera. Those may enter the re-circulation zone, and transported by a cross-flow to the centre were observed. It would indicate existence of a strong cross-flow in this region that in fact partially was observed in our velocity field measurements.

3. Visualization of liquid jet break-up and droplet formation for co-flow

Visualization of liquid jet break-up and droplet formation for co-flow in the geometry G3 is investigated under the microscope using 4x objective and PCO HS1200 camera. The corresponding scale for images is 1pixel = 3.012μm or 1μm = 0.332pixel. The carrier fluid is supplied with controlled flow rate Q_e to the horizontally orientated channel. Silicon oil is injected coaxially at the flow rate Q_j to create a liquid jet. To avoid effects of buoyancy water-alcohol mixture is used as the carrier fluid. The water:alcohol volume ratio necessary to match densities of continuous and dispersed phase is approximately 5:2. To stabilize surface tension effects 1%wt anionic surfactant sodium dodecyl sulphate (SDS) was added to the carrier fluid. Two different silicone oils were used to change the droplet phase viscosity: S50 (50mPas) and S500 (500mPas). Table 3.1 summarizes range of varied flow rate and gives the corresponding average velocity for continuous (external) and dispersed (jet) phase.

Table 3.1. Jet break-up study. The mean flow velocities V_e and V_j are based on the channel cross-section and inner nozzle diameter, respectively.

Oil	Q_e [cm^3/s]	V_e [cm/s]	Q_j [mm^3/s]	V_j [mm/s]
S50 (50mPas)	1.08 - 3.57	2.16 – 7.14	22 – 33	112.2 – 168.3
S500 (500mPas)	0.92 – 1.72	1.84 - 3.44	5.5 –33	28.1 - 168.3

The liquid jet observed in the channel showed basic similarities to typical jet instabilities described for air-liquid systems. At lower viscosity of the dispersed phase (S50) the jet issuing from the nozzle at relatively low velocity created tiny neck and shortly after it broke-up creating large droplet and a sequence of very small satellites (Fig. 3.1). The characteristic thin filament was present before droplet separated. This thin micro-jet reached diameter of about 1μm before the break-up occurred. The resulting satellite droplets had diameters below 5μm. When the jet flow rate increased from $22mm^3/s$ to $33mm^3/s$, the break-up process slightly changed. The jet break-up period decreased from 60ms to 50ms and the visible jet neck doubled its length before droplet separation occurred. Also the thin filament length reached over 1.5mm before it broke-up into several satellites.

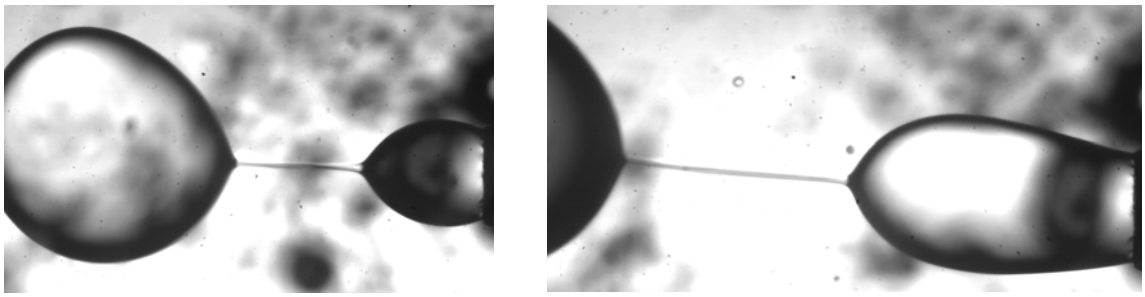

a b

Figure 3.1. Silicone oil jet S50. (a) - oil injected at flow rate $Q_j = 22mm^3/s$ into water-alcohol channel flow at the rate $Q_e = 1.08cm^3/s$. The break-up period is 60ms; (b) - $Q_j = 33mm^3/s$ and $Q_e = 1.08cm^3/s$ The width of images corresponds to 3.6mm.

The external flow strongly interacted with the jet and initial increase of the co-flow velocity damped capillary instability and allowed to obtain long, cylindrical jet (Fig. 3.2a). However, short length of the channel created irregularities in the co-flow pattern and generation of recalculation regions. These external flow fluctuations strongly disturbed the jet interface, leading to its wave shape, irregular break-up and creation of secondary, thin filaments

(Fig. 3.2b). The filaments break-up resembles process observed for droplets processed in the emulsifier.

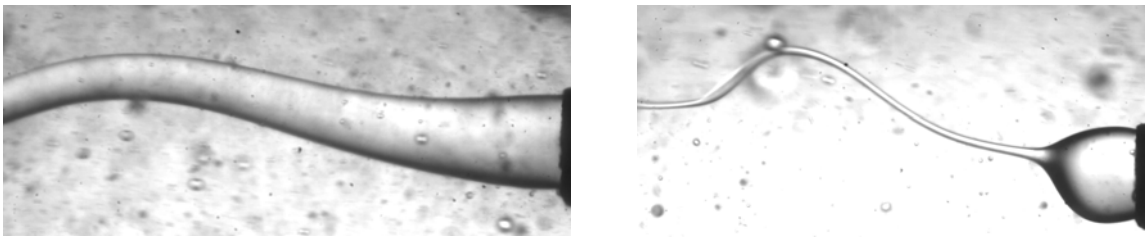

a b

Figure 3.2. Silicone oil jet S50. Oil injected at flow rate Q_j = 33mm^3/s into water-alcohol channel flow at the rate Q_e = 2.7cm^3/s. The jet break-up is driven by shear stresses at the interface.

The experiments performed for 10-fold more viscous oil (S500) indicated higher damping of capillary instability. At higher jet velocity a long, slowly pulsating cylindrical jet was formed (Fig. 3.3a). The capillary wave observed at the interface had period of about 60ms. The break-up point was far from the nozzle. At lower flow rates of the injected oil, the separation of a droplet commences at a short distance from the nozzle. However, due to the very high viscosity of the jet fluid, very long thin filament was created between remaining part of the jet and departing droplet (Fig. 3.3b). The break-up period recorded for this case was very long (240ms). Further decrease of the oil velocity (Q_j < 10mm^3/s) leads to the "filling mode", i.e. oil continuously filled up the channel section in the vicinity of the nozzle. There was no jet structure and collected in the channel bulk oil was time-to-time partially removed by the continuous phase flow.

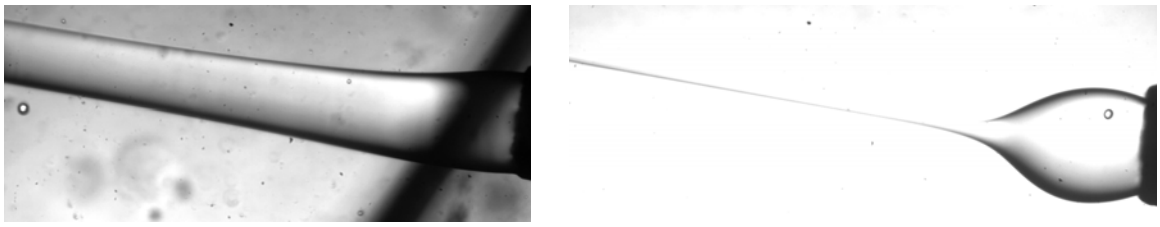

a b

Figure 3.3. Silicone oil jet S500. a - oil injected at flow rate Q_j = 33mm^3/s into water-alcohol channel flow at the rate Q_e = 1.3cm^3/s, the period of observed capillary wave 60ms.; b – thin filament shortly before droplet separation (outside the area of observation), Q_j = 14mm^3/s, Q_e = 1.47cm^3/s, the break-up period 240ms.

The conclusions from the experiments performed for two different viscosities are as following:

For the less viscous liquid the capillary instability seems to play a role at low velocity of the continuous phase. At higher velocities disturbances of the flow in the channel lead to "turbulent-like" flow structure with several recirculation zones. This perturbation can be used to study break-up mechanism at a turbulent shear flow field.

At higher liquid viscosity it is difficult to reach stable configuration corresponding to capillary (Rayleigh-like) break-up process. This probable due to relatively long minimum wavelength of the most unstable mode, comparable with the size of the channel. Hence at higher flow rates the jet appears very stable (Fig. 3.3a). For lower jet velocities the droplets are created close to the nozzle and convected by the external flow field. It creates extremely long detachment filaments (Fig. 3.3b). Break-up of these filaments is probably the most promising source of micro- and nano-droplets searched for in the present study.

4. Numerical simulation of the flow through the planar emulsifier

4.1 Geometry configuration and mesh parameters

For numerical simulations three different geometries of the planar emulsifier were defined:

1. G0 – whole geometry of the model (Fig. 4.1) with transparent processing element (gap size: width 15mm, height 0.4mm and length 2mm);
2. G1-v1[1] – one quarter of the model (Fig. 4.2c) with non-transparent processing element (gap size: width 15mm, height 0.4mm and length 1mm);
3. G2 – one quarter of the model (Fig. 4.2a,b) with transparent processing element (gap size: width 15mm, height 0.4mm and length 2mm).

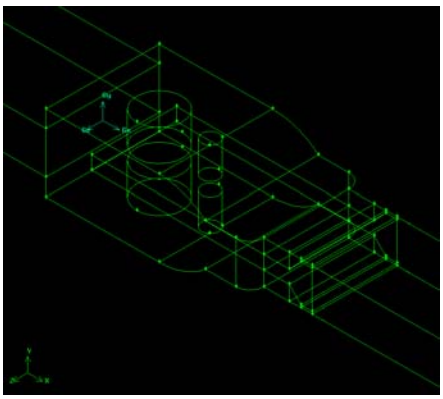

(a)

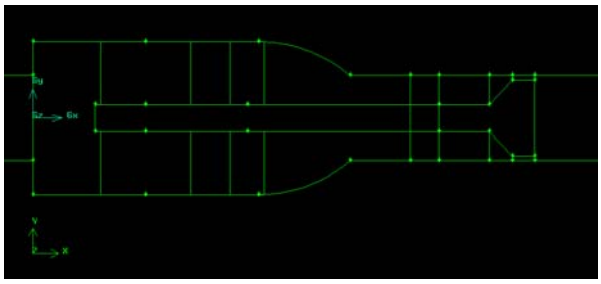

(b)

Figure 4.1. Geometry G0 of the planar emulsifier: isometric (a) and side view (b).

Geometry G0 consists of 1820957 cells, 5190188 faces and 1599368 nodes. In the gaps and in the vicinity of the gap was generated structural hexahedron mesh and in the other parts of the geometry – tetrahedron mesh (Fig. 4.3).

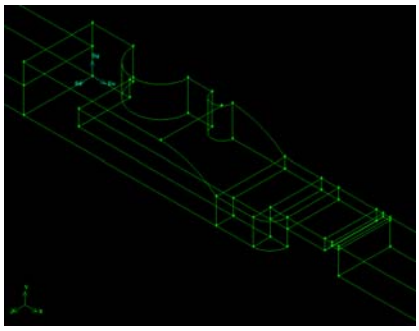

(a)

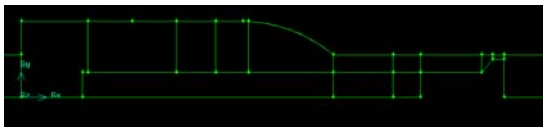

(b)

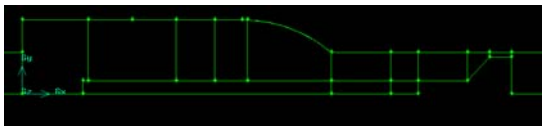

(c)

Figure 4.2. Geometry G1 of the planar emulsifier: isometric (a) and side view (b) and side view of the geometry G2 (c).

Geometry G1 and geometry G2 consists of 457473 cells, 1189395 faces and 302334 nodes. In the gap and in the vicinity of the processing element was generated structural hexahedron

[1] Modified geometry G1 (height of the channel before processing element: 1.5mm)

mesh with boundary layer (Fig. 4.4a and 4.4b for geometry G1 and G2 respectively) and in the other parts of the geometry – tetrahedron mesh.

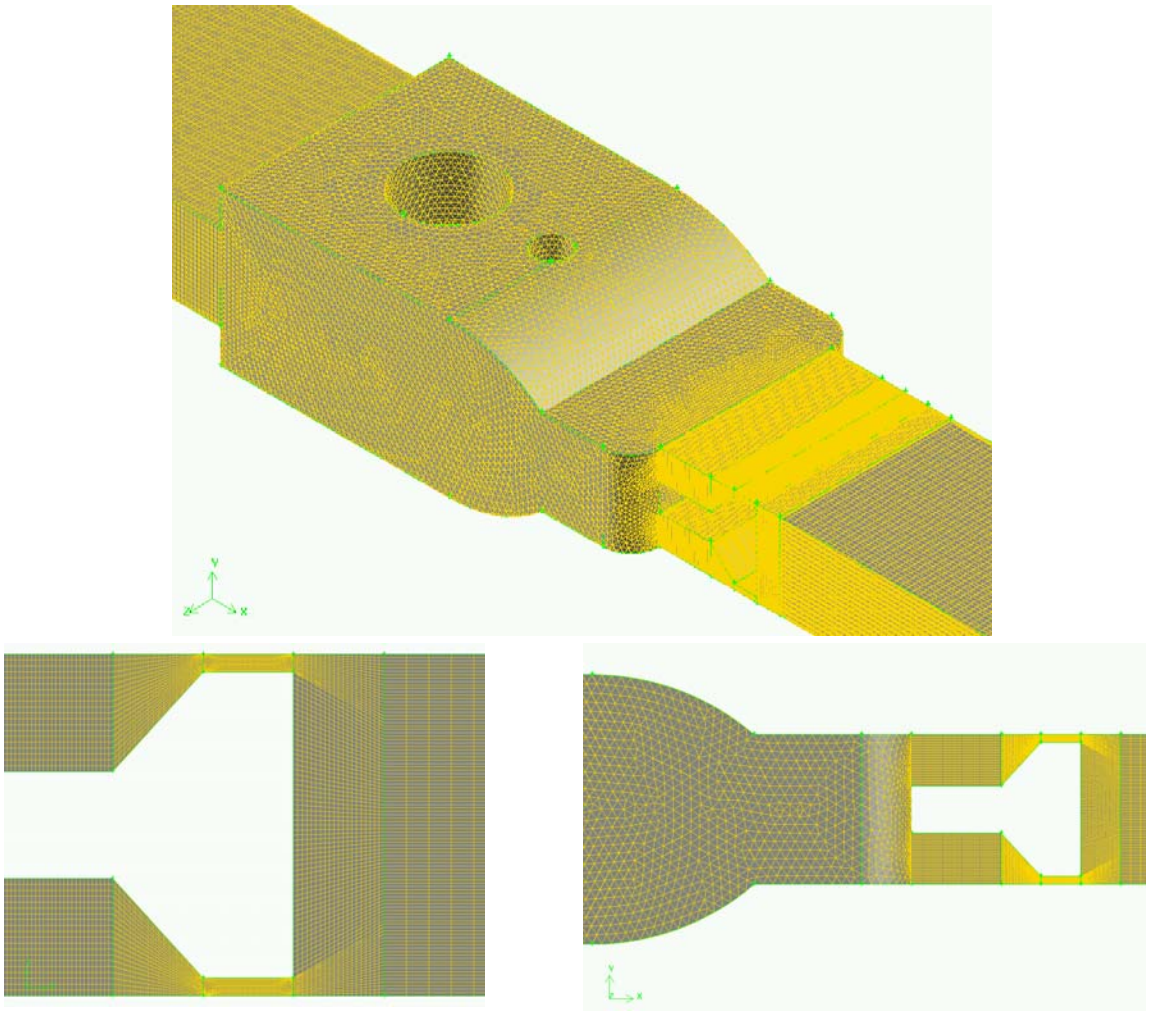

Figure 4.3. Geometry G0 – mesh used for numerical simulation.

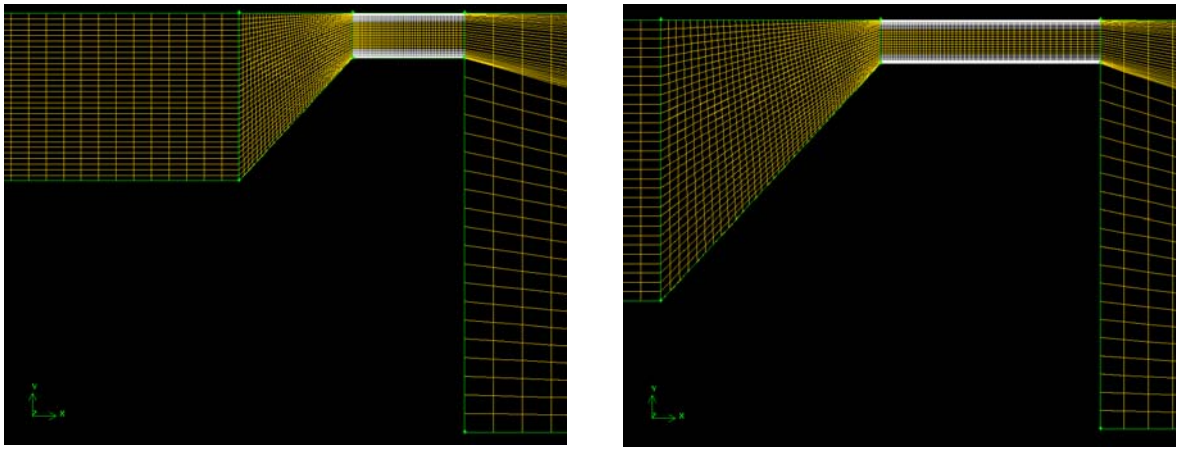

(a) (b)

Figure 4.4. Mesh with boundary layer in the gap: a) geometry G2, b) geometry G1.

4.2 Numerical simulation

Using geometry G0 two numerical simulations were done (both for planar emulsifier with transparent processing element):

a. flow rate $Q_a = 0.13\ dm^3/s$
b. flow rate $Q_b = 0.204\ dm^3/s$.

The parameters of these numerical simulations collect table 4.1.

Table 4.1. Parameters of the numerical simulations of turbulent flow through emulsifier with transparent processing element – geometry G0.

	$Q_a = 0.13\ dm^3/s$	**$Q_b = 0.204\ dm^3/s$**
Used package and version	Fluent 6.2.16, double precision, segregated	
Flow type	three-dimensional, steady, incompressible	
Viscosity model	standard k – ε turbulence model	
Medium	water, constant density ρ= 998.2 *kg/m³* and viscosity μ=0.001003 *kg/ms*	
Mass flow-rate	0.13 *kg/s*	0.2306 *kg/s*
Inlet	mass-flow inlet, turbulence intensity 12.1% hydraulic diameter 0.0109	mass-flow inlet, turbulence intensity 11.4% hydraulic diameter 0.0109
Outlet	pressure outlet, turbulence intensity 12.1% hydraulic diameter 0.0109	pressure outlet, turbulence intensity 11.4% hydraulic diameter 0.0109
Discretization Scheme	Pressure: standard Momentum: Second Order Upwind Turbulence Kinetic Energy: Second Order Upwind Turbulence Dissipation Rate: Second Order Upwind	

For flow rate $Q_b = 0.204\ dm^3/s$ using geometry G1 and G2 (emulsifier with non-transparent and transparent processing element) following simulations were done:

- **g1lam** and **g2lam** – laminar unsteady flow simulations through emulsifier with non-transparent and transparent processing element respectively,
- **g1ke** and **g2ke** – simulation of the steady turbulent flow through emulsifier with non-transparent and transparent processing element respectively using k-ε turbulence model with Enhanced Wall Treatment on the walls in the gap and vicinity of the gap; additionally was used grid adaptation based on the gradient of velocity magnitude (refine threshold 0.0001) and Yplus parameter (allowed value: 1 – 2).

Tables 4.2 and 4.3 collect parameters for laminar and turbulent simulations respectively.

Table 4.2. Parameters of the numerical simulations of laminar flow through emulsifier with non-transparent and transparent processing element – geometry G1 and G2.

	Geometry G1 and G2 (g1lam and g2lam)
Used package and version	Fluent 6.2.16, double precision, segregated
Flow type	three-dimensional, laminar, unsteady, incompressible
Medium	water, constant density ρ= 998.2 *kg/m³* and viscosity μ=0.001003 *kg/ms*

Mass flow-rate	0.051 *kg/s* (one quarter of Q=0.204 *kg/s*)
Inlet	mass-flow inlet
Outlet	pressure outlet
Discretization Scheme	Pressure: standard Momentum: Second Order Upwind
Time Step Size	$1e^{-7}$ s

Table 4.3. Parameters of the numerical simulations of turbulent flow through emulsifier with non-transparent and transparent processing element – geometry G1 and G2.

	Geometry G1 and G2 (g1ke and g2ke)
Used package and version	Fluent 6.2.16, double precision, segregated
Flow type	three-dimensional, steady, incompressible
Viscosity model	standard k – ε turbulence model with Enhanced Wall Treatment
Medium	water, constant density ρ= 998.2 *kg/m*^{3} and viscosity μ=0.001003 *kg/ms*
Mass flow-rate	0.051 *kg/s* (one quarter of Q=0.204 *kg/s*)
Inlet	mass-flow inlet turbulence intensity 12.1% hydraulic diameter 0.0109
Outlet	pressure outlet turbulence intensity 12.1% hydraulic diameter 0.0109
Discretization Scheme	Pressure: standard Momentum: Second Order Upwind Turbulence Kinetic Energy: Second Order Upwind Turbulence Dissipation Rate: Second Order Upwind
Grid Adaptation	dynamic adaptation based on velocity magnitude gradient: refine threshold 0.0001, interval: 20 iterations Yplus: allowed value 1 – 2

4.3 Numerical simulations results for geometry G0.

Figures presented in this chapter show results of the numerical simulation of the flow through emulsifier model – geometry G0 (transparent processing element) with two flow rates: $Q_a = 0.13$ *dm*^{3}*/s* and $Q_b = 0.204$ *dm*^{3}*/s*.

For results presentation four sections was defined (Fig. 4.5):

- vertical – longitudinal section along emulsifier model,
- vertical – cross section 5.5mm before processing element (cross-section I),
- vertical – cross section in the middle of the gap (cross-section II),
- vertical – cross section 9.5mm behind processing element (cross-section III).

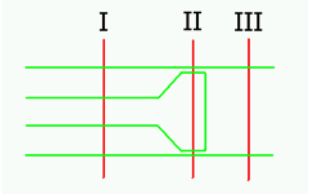

Figure 4.5. Selected cross-sections: I – 5.5*mm* before processing element, II – in the middle of the gap, III – 9.5*mm* behind processing element.

Figure 4.6 shows longitudinal section along emulsifier model of the velocity vectors field in the gaps and in the space behind processing element for flow rates $Q_a = 0.13\ dm^3/s$ (Fig. 4.6a) and $Q_b = 0.204\ dm^3/s$ (Fig. 4.6b). Vectors are coloured by velocity magnitude. For both cases flow fields are very similar in structure, differences occur in velocity value, only. For flow rate $Q_a = 0.13\ dm^3/s$ maximum velocity is about $12 m/s$ in the gaps and for $Q_b = 0.204\ dm^3/s$ about $20 m/s$. Strong recirculation zone and reverse flow in the space behind processing element are significant in this region of the emulsifier and can influence oil-droplets break-up process.

a)

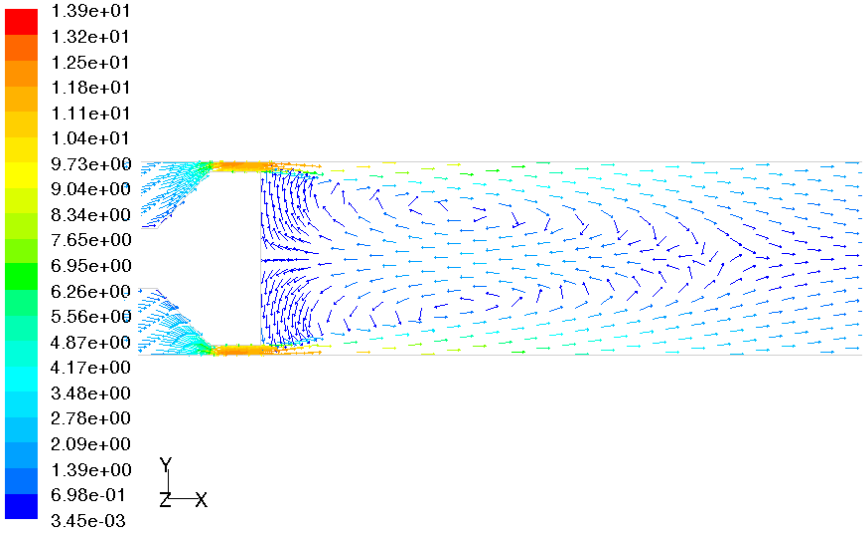

b)

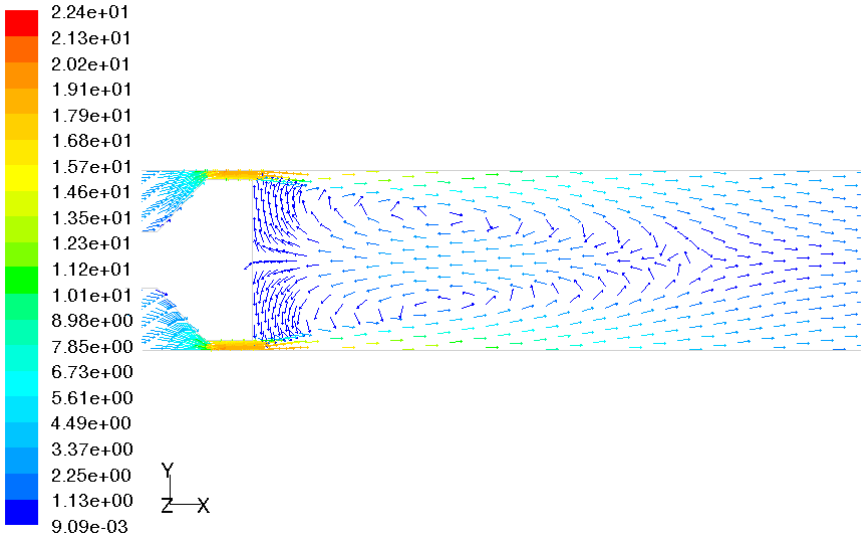

Figure 4.6. Velocity vectors in the vicinity of the processing element [m/s]: a) $Q_a = 0.13\ dm^3/s$, b) $Q_b = 0.204\ dm^3/s$.

Contours of the velocity magnitude shown in the figure 4.7 confirm similarity of the flow structure in the vicinity of the processing element for both flow rates. Additionally it was noticed that flow velocity in the region before gaps was very low and flow acceleration occurs in the gaps between processing element and walls, mainly.

a)

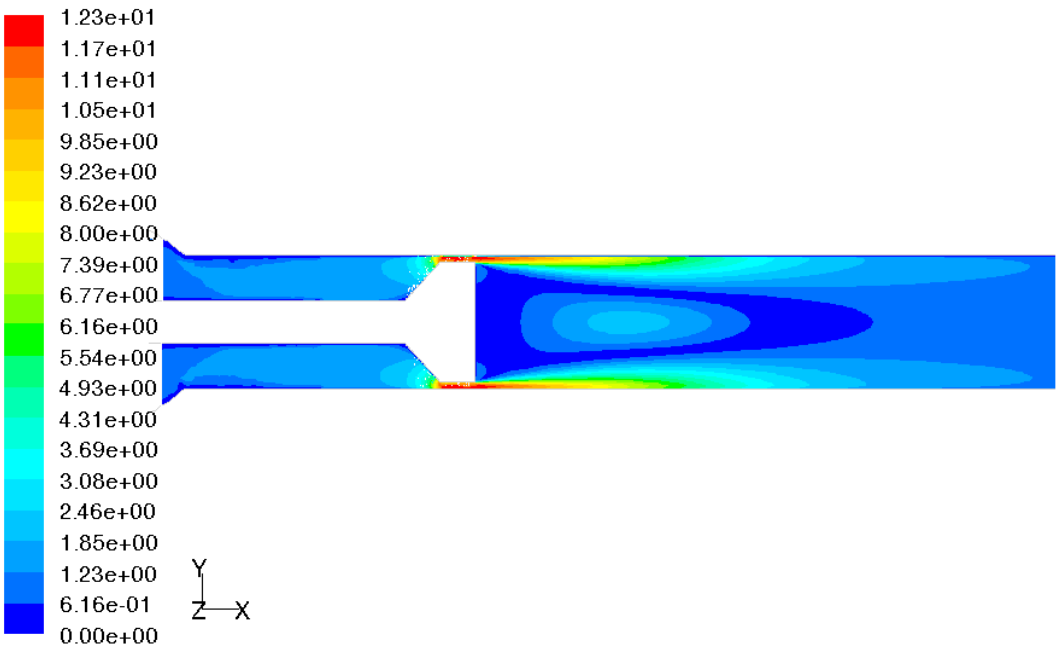

b)

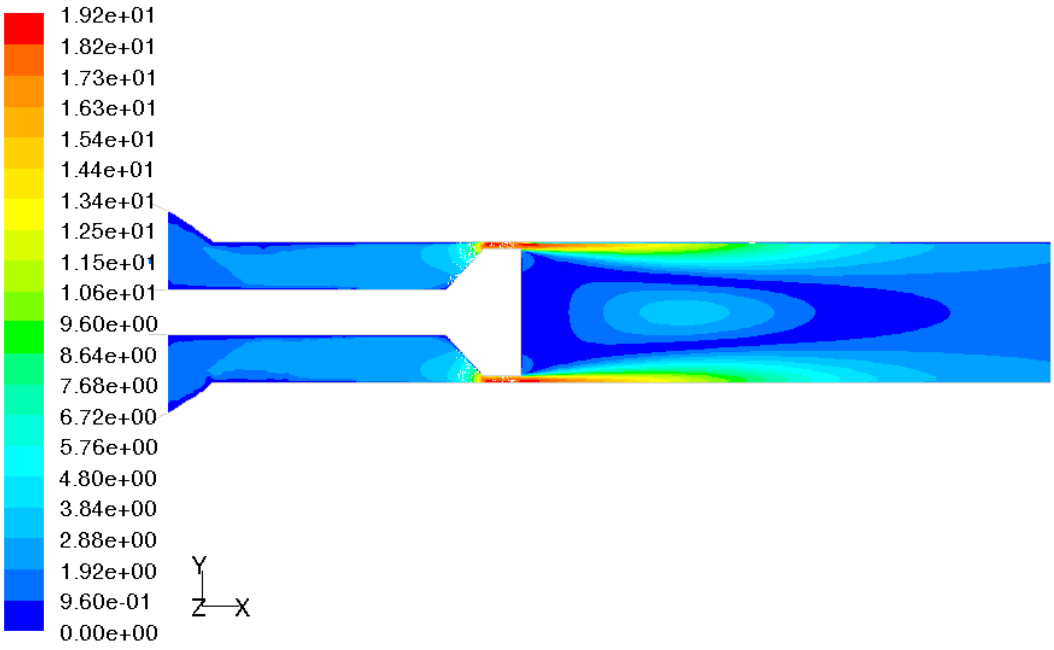

Figure 4.7. Contours of velocity magnitude [*m/s*]: a) $Q_a = 0.13\ dm^3/s$, b) $Q_b = 0.204\ dm^3/s$.

Similarly, as it is shown in the figure 4.8, cross-sections of the velocity magnitude contours are almost identical for flow rates $Q_a = 0.13$ dm^3/s (Fig. 4.8a) and $Q_b = 0.204$ dm^3/s (Fig. 4.8b).

a)

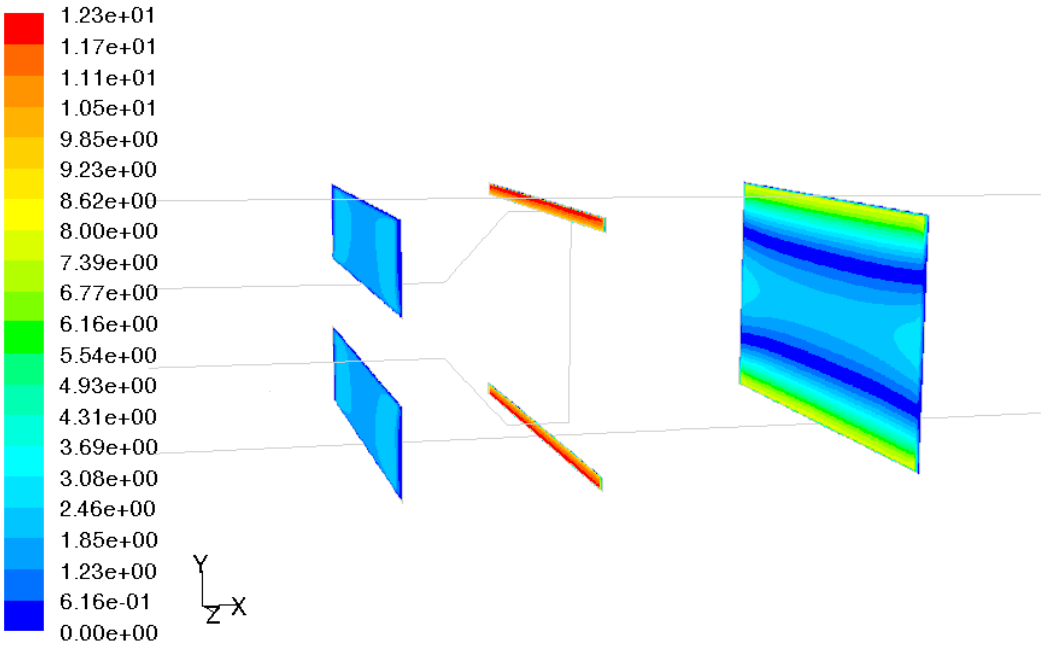

b)

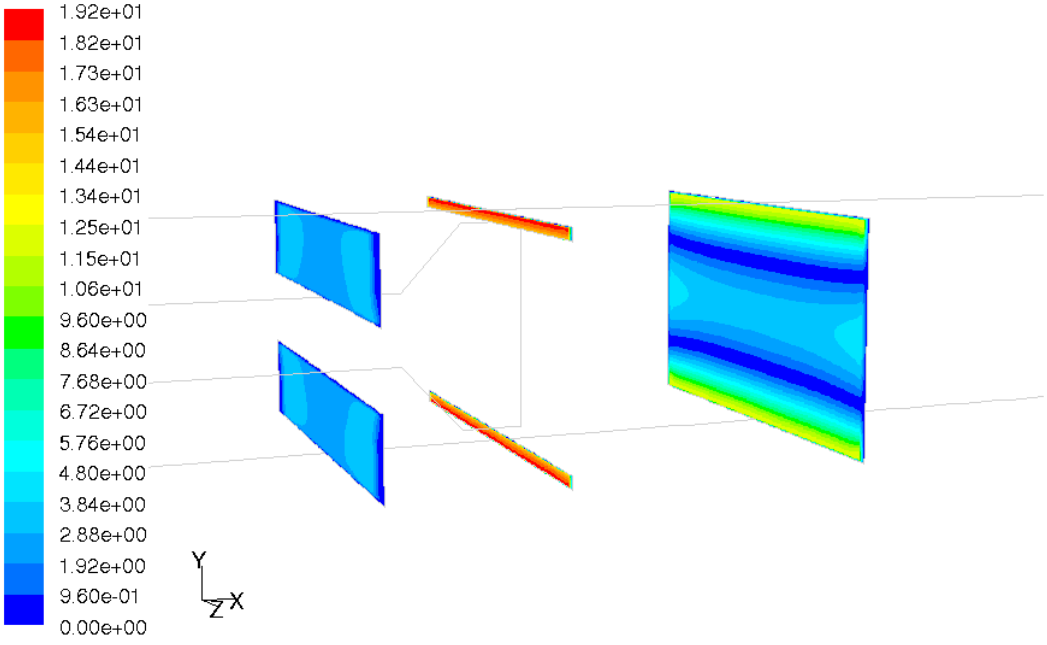

Figure 4.8. Contours of velocity magnitude – selected cross-sections [*m/s*]: a) $Q_a = 0.13$ dm^3/s, b) $Q_b = 0.204$ dm^3/s.

Figure 4.9 shows longitudinal section of the velocity x-component along emulsifier model. Backflow in the region behind processing element is significant and for the flow rate $Q_a = 0.13\ dm^3/s$ is about -2*m/s* (blue area behind processing element in the Fig. 4.9a) and for $Q_b = 0.204\ dm^3/s$ is about -4*m/s* (Fig. 4.9b).

a)

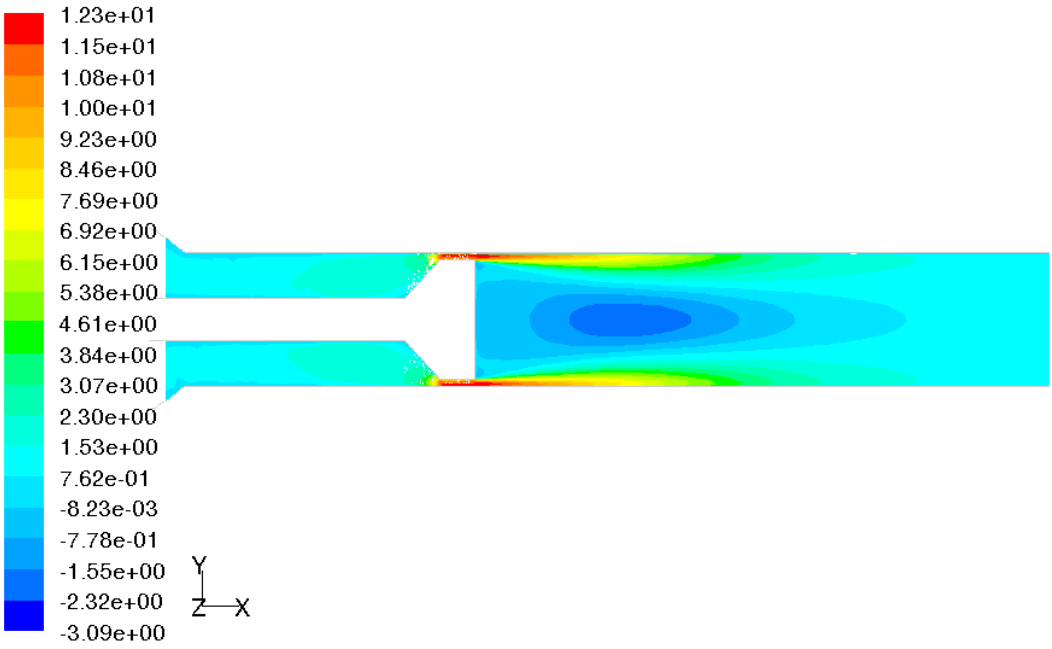

b)

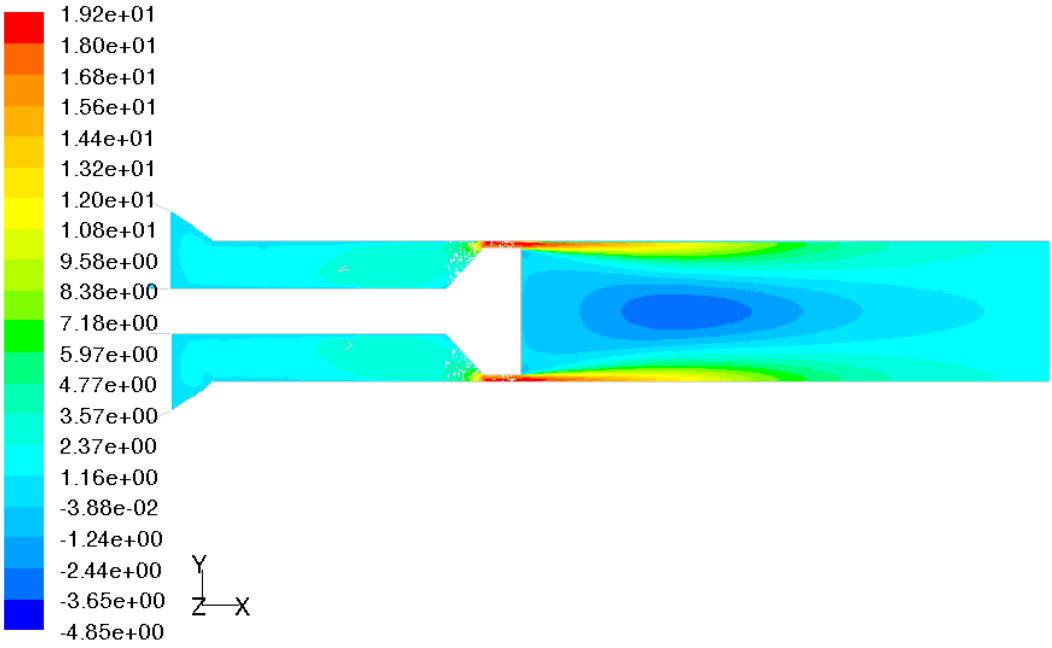

Figure 4.9. Contours of velocity x-component [*m/s*]: a) $Q_a = 0.13\ dm^3/s$, b) $Q_b = 0.204\ dm^3/s$.

Contours of the absolute pressure (Fig. 4.10) shows that pressure drop occurs mainly in the same place where flow is accelerated, i.e. in the gaps between processing element and walls. Pressure for flow rate $Q_a = 0.13\ dm^3/s$ decreases from value about $1.83 \cdot 10^5 Pa$ before the gaps to atmospheric pressure (about $10^5 Pa$) at the outlet (Fig. 4.10a) and for flow rate $Q_b = 0.204\ dm^3/s$ decrease from $3 \cdot 10^5 Pa$ to atmospheric pressure at the outlet (Fig. 4.10b).

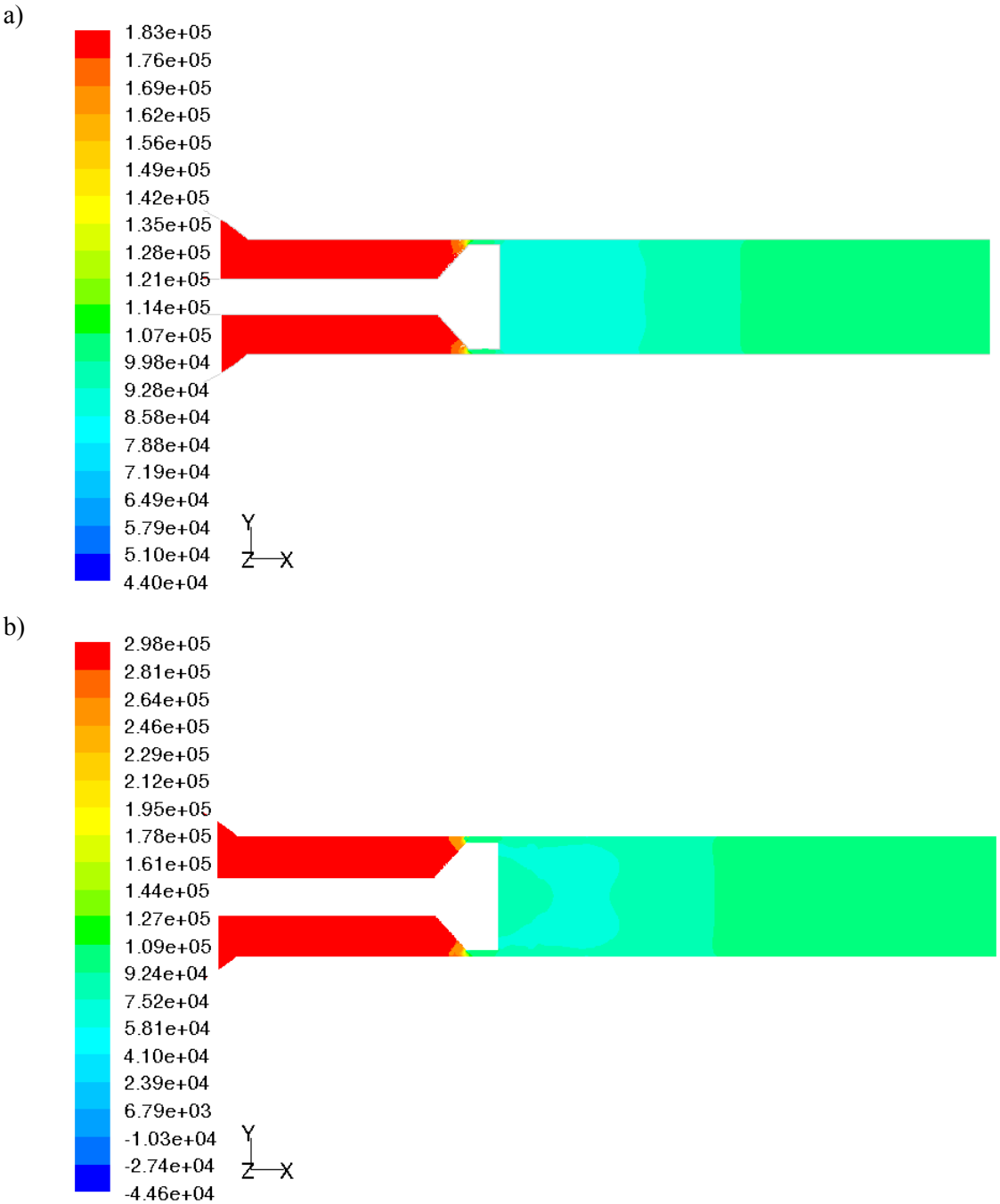

Figure 4.10. Contours of absolute pressure [*Pa*]: a) $Q_a = 0.13\ dm^3/s$, b) $Q_b = 0.204\ dm^3/s$.

Figure 4.11 shows turbulent kinetic energy distribution along emulsifier model. For both cases this energy reaches maximum value at the inlet to the gaps: for flow rate $Q_a = 0.13\ dm^3/s$ it is $k_a = 12 m^2/s^2$, and for $Q_b = 0.204\ dm^3/s$ it is $k_b = 32 m^2/s^2$. Also, turbulent kinetic energy takes high value in the regions behind processing element, where occurs mixing of the fluid with high velocity value flowed from gaps and fluid with low velocity value behind processing element.

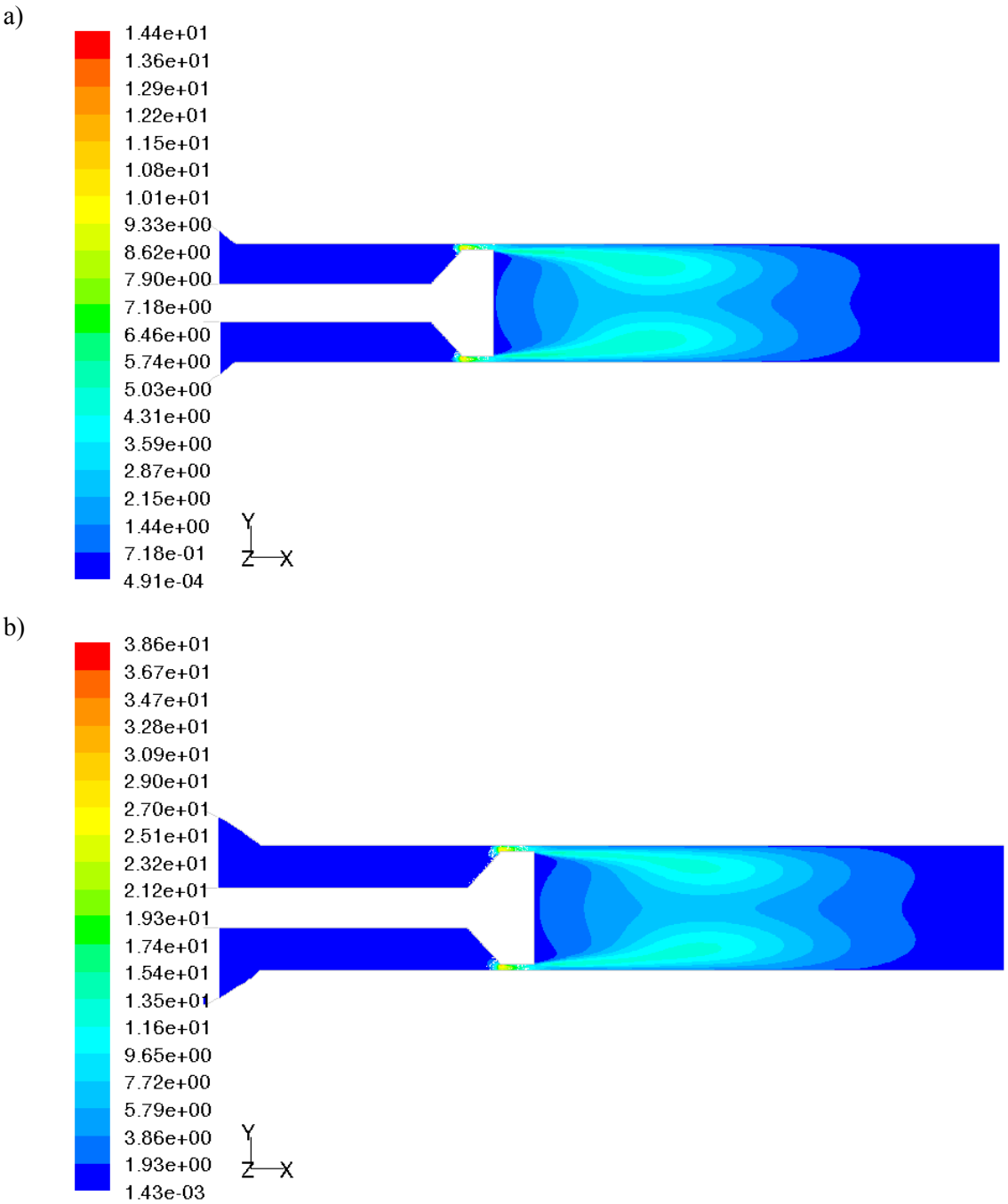

Figure 4.11. Contours of Turbulent Kinetic Energy [m^2/s^2]: a) $Q_a = 0.13\ dm^3/s$, b) $Q_b = 0.204\ dm^3/s$.

Profiles in the figure 4.12 shows averaged turbulent dissipation rate ε along the gap for both flow rates: $Q_a = 0.13\ dm^3/s$ (Fig. 4.12a) and $Q_b = 0.204\ dm^3/s$ (fig 4.12b).
Turbulent dissipation rate reaches maximum value at the inlet to the gap, as it is shown. For flow rate Q_a this maximum value is about $\varepsilon_a^{max} = 1.84 \cdot 10^5 m^2/s^3$ and for Q_b about $\varepsilon_b^{max} = 5.59 \cdot 10^5 m^2/s^3$.
Epsilon averaged over the whole gap is: $\varepsilon_a^{avg} = 7.29 \cdot 10^4 m^2/s^3$ and $\varepsilon_b^{avg} = 2.65 \cdot 10^5 m^2/s^3$ for flow rate Q_a and Q_b respectively.

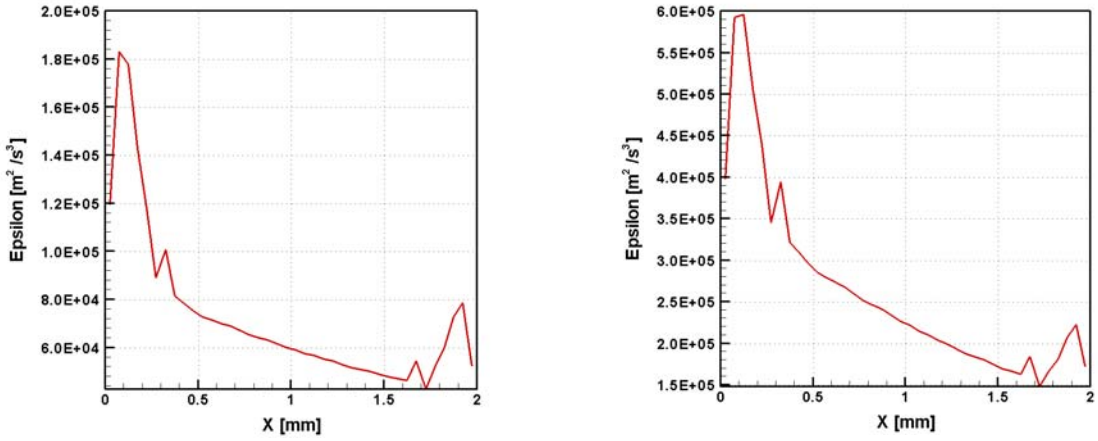

(a) (b)

Figure 4.12. Profile of the averaged Turbulent Dissipation Rate *Epsilon* through the gap:
a) $Q_a = 0.13\ dm^3/s$, b) $Q_b = 0.204\ dm^3/s$.

4.4 Numerical simulations results for geometry G1 and G2 (simulations g1ke and g2ke)

Presented in this chapter figures show results of the numerical simulation of the flow through emulsifier model with geometry G1 and G2 (non-transparent and transparent processing element, respectively) for flow rate Q = 0.204 dm^3/s.
For results presentation, like in the chapter 4.3, four sections was defined (Fig. 4.5):

- vertical – longitudinal section along emulsifier model,
- vertical – cross section 5.5mm before processing element (cross-section I),
- vertical – cross section in the middle of the gap (cross-section II),
- vertical – cross section 9.5mm behind processing element (cross-section III).

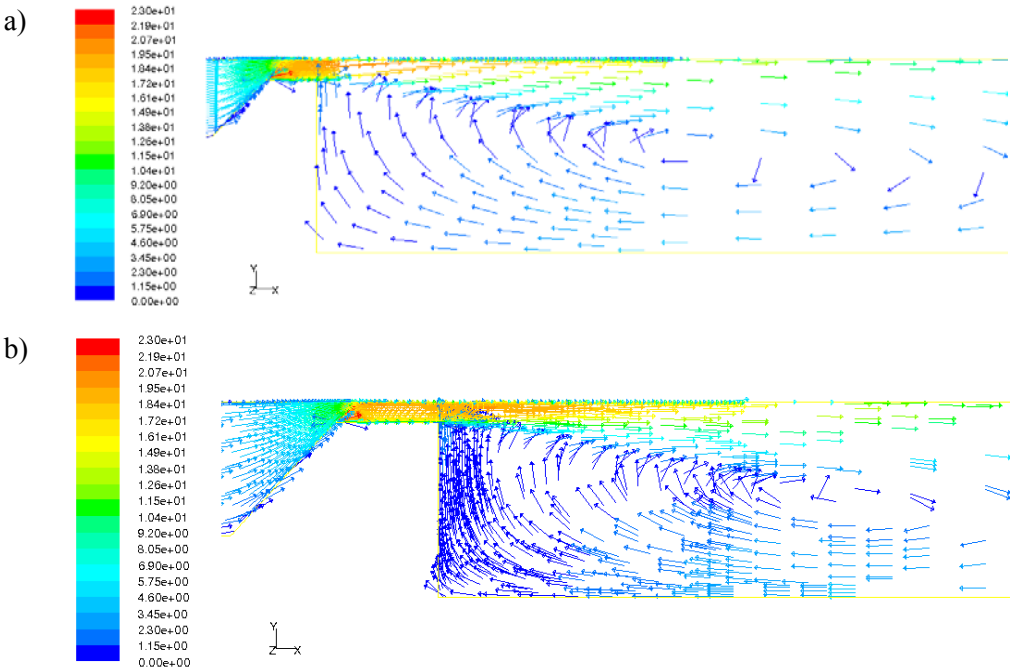

Figure 4.13. Velocity vectors in the vicinity of the processing element [*m/s*]: a) simulation g1ke, b) simulation g2ke.

Figure 4.13 shows longitudinal section along emulsifier model of the velocity vectors field in the gap and in the region behind processing element for emulsifier with transparent (Fig. 4.13a) and non-transparent (Fig. 4.13b) processing element. For both cases flow fields are very similar in structure and in the velocity value (vectors colour).
This is confirmed by next figure 4.14 that shows contours of the velocity magnitude. For both cases (Fig. 4.14a and 4.14b) maximum velocity is in the gap between processing element and walls and has value about 20*m/s*.
Cross-sections of the velocity magnitude presented in the figure 4.15 are almost identical for emulsifier geometry G1 and G2. It proves that differences in flow structure and velocity value for both used geometries are very small.

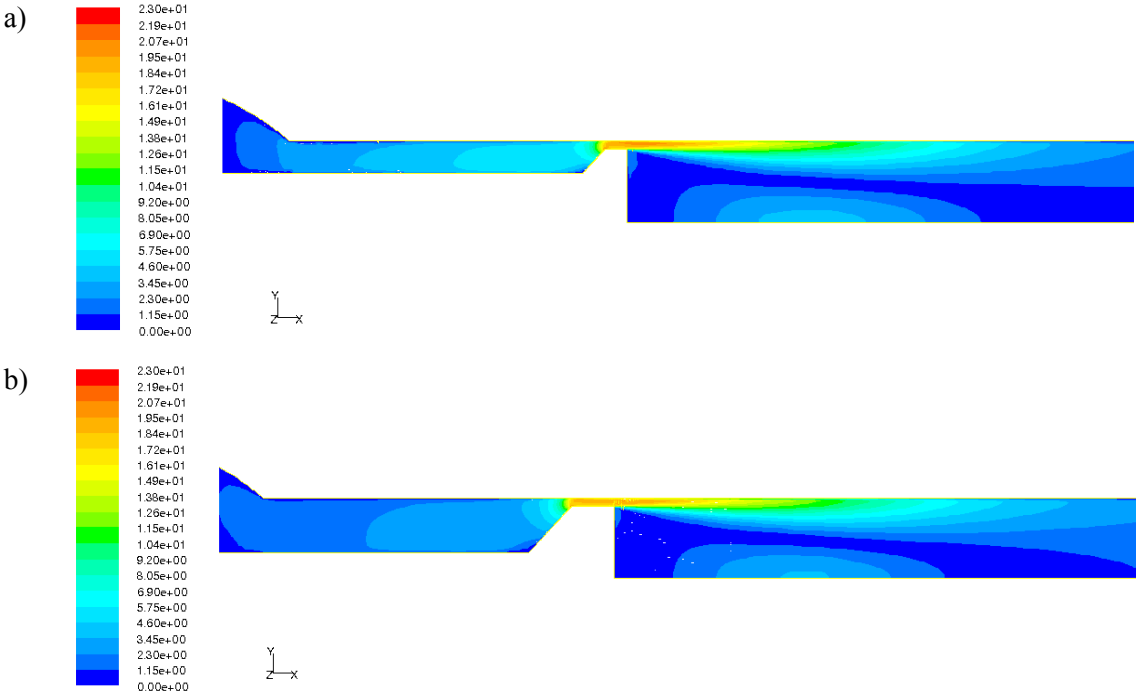

Figure 4.14. Contours of velocity magnitude [*m/s*]: a) simulation g1ke, b) simulation g2ke.

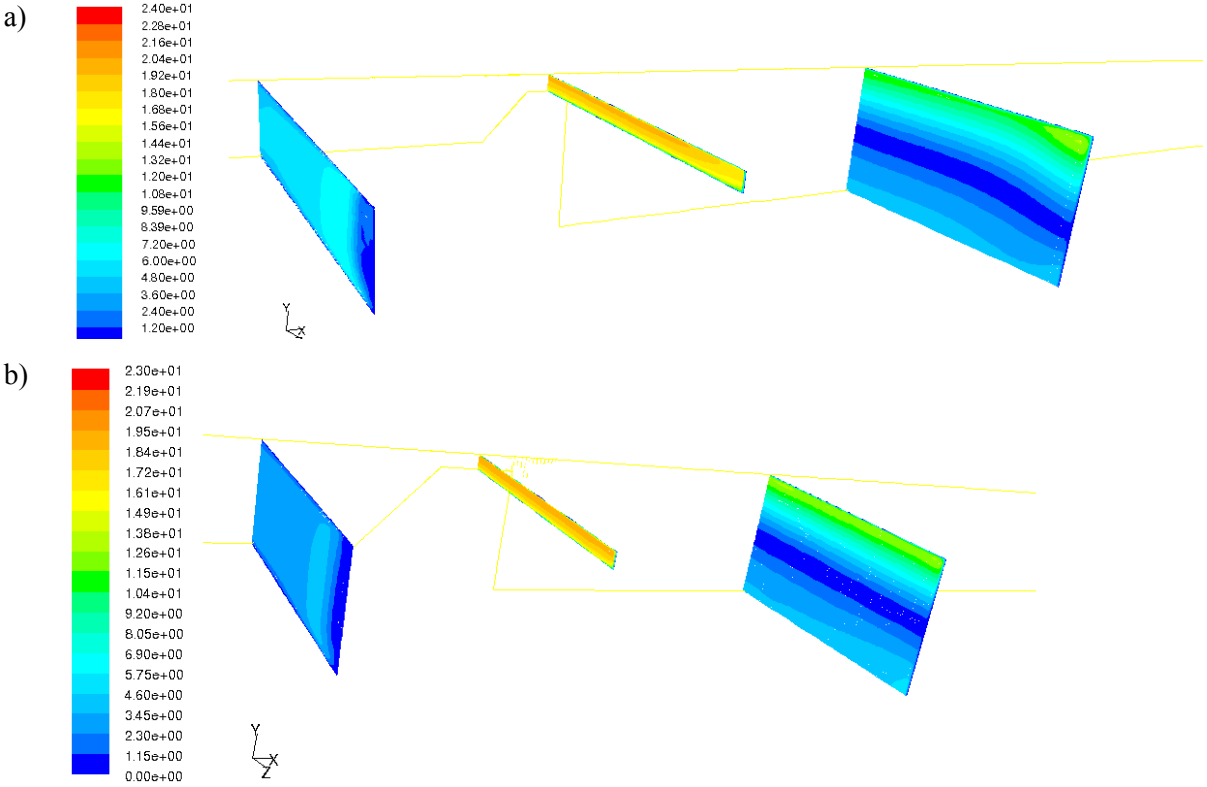

Figure 4.15. Contours of velocity magnitude – selected cross-sections [*m/s*]: a) simulation g1ke, b) simulation g2ke.

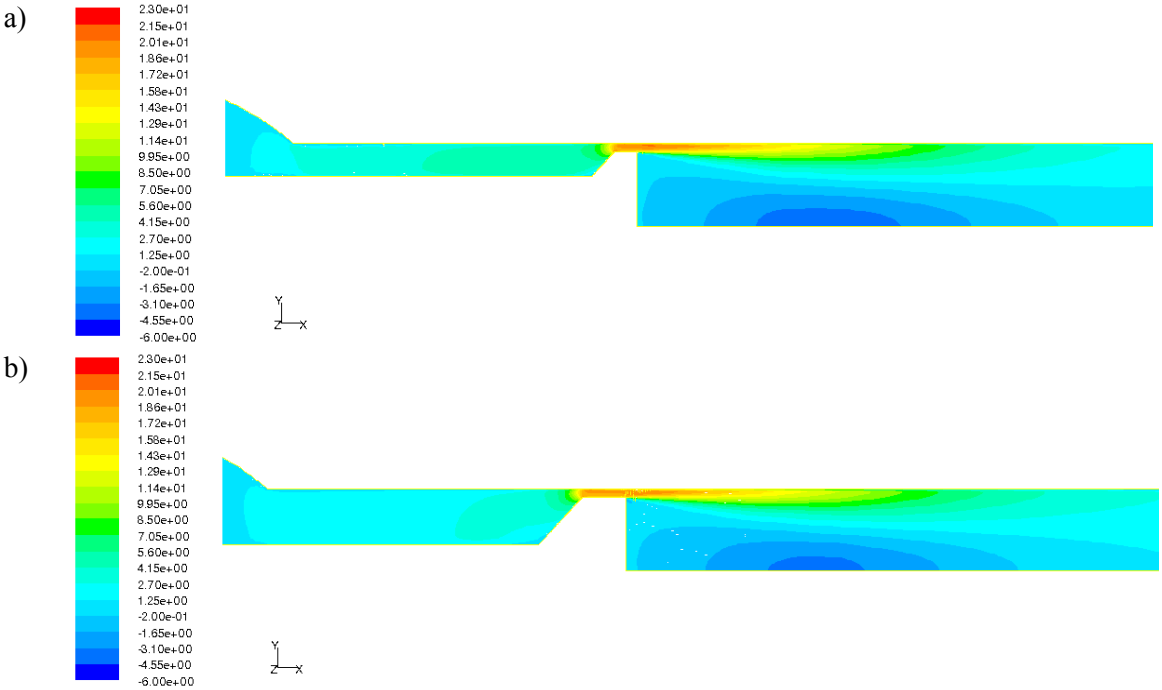

Figure 4.16. Contours of velocity x-component [*m/s*]: a) simulation g1ke, b) simulation g2ke.

Figure 4.16 shows longitudinal section along emulsifier model of the velocity x-component for geometry G1 and G2. For both cases backflow in the region behind processing element is significant. Velocity value of this reverse flow is about -5*m/s* (blue area behind processing element). Velocity in the gap is about 20*m/s*.

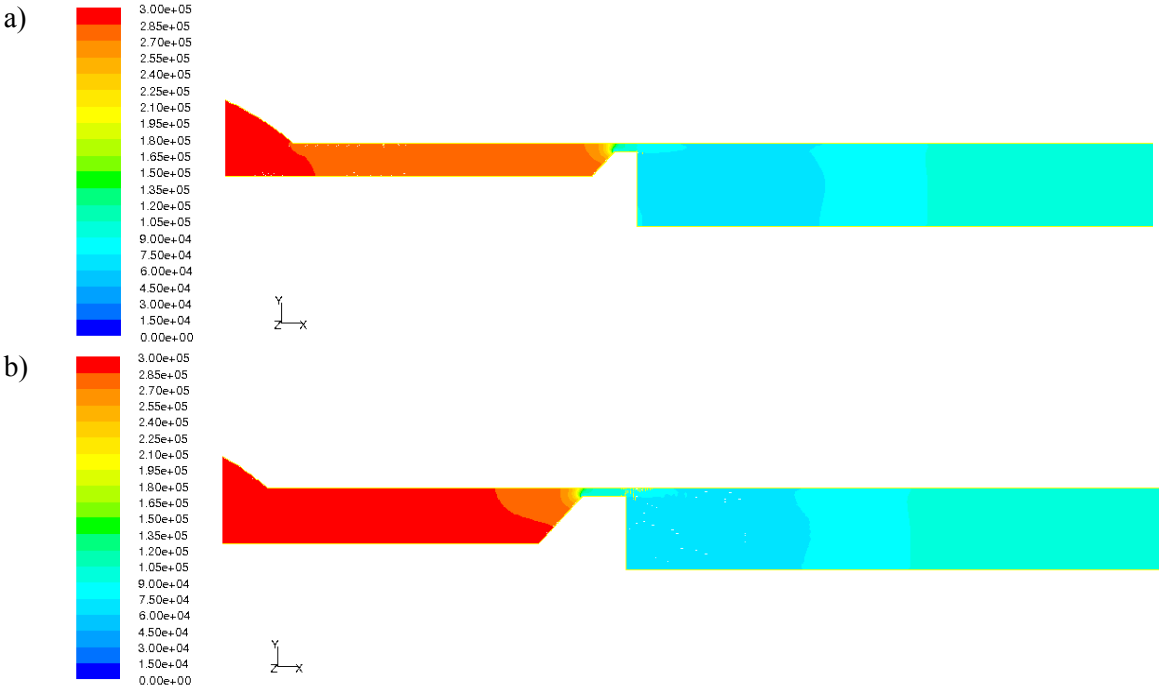

Figure 4.17. Contours of absolute pressure [*Pa*]: a) simulation g1ke, b) simulation g2ke.

Contours of the absolute pressure presented in figure 4.17 shows that pressure drop occurs in the gap, mainly. Pressure decreases at this point from $3 \cdot 10^5 Pa$ to atmospheric pressure

($10^5 Pa$). Also, it can be noticed, that distribution of the absolute pressure for both geometries: with non-transparent and transparent element (geometry G1 and G2) are very similar.

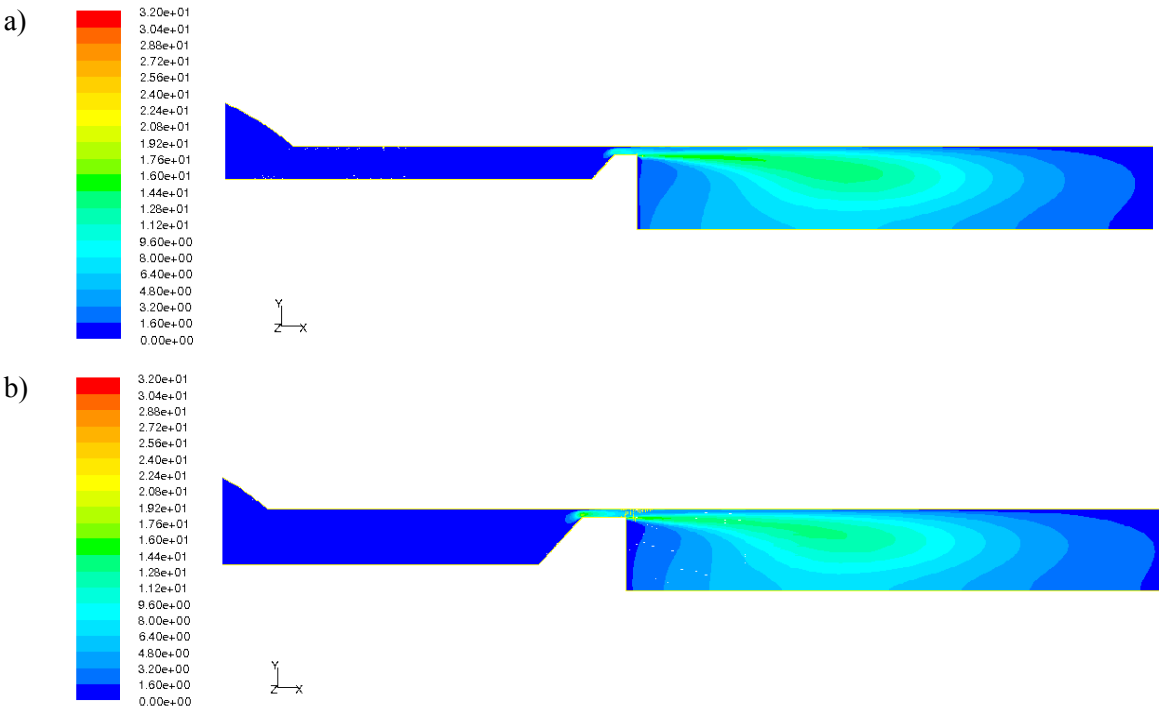

Figure 4.18. Contours of Turbulent Kinetic Energy [m^2/s^2]: a) simulation g1ke, b) simulation g2ke.

Distribution of the turbulent kinetic energy (Fig. 4.18) shows that maximum value is reached in the region behind processing element, where occurs mixing of the fluid with high velocity value flowed from gap and fluid with low velocity value behind processing element. Differences in turbulent kinetic energy distribution for geometry G1 (Fig. 4.18b) and geometry G2 (Fig. 4.18a) are very small.

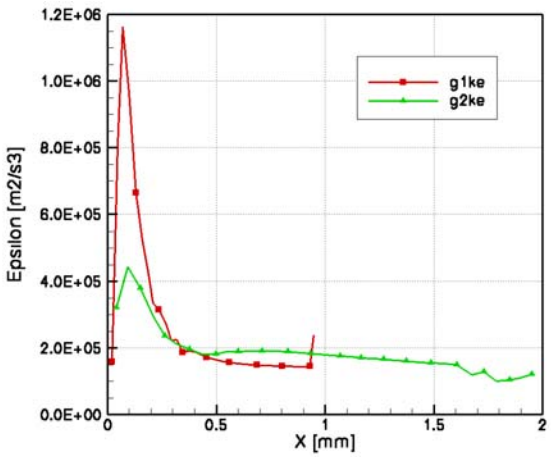

Figure 4.19. Horizontal profile of the averaged Turbulent Dissipation Rate *Epsilon* through the gap for emulsifier with non-transparent (g1ke) and transparent (g2ke) processing element.

Profiles presented in figure 4.19 shows averaged turbulent dissipation rate (Epsilon) distribution along the gap for geometry G1 (green line) and for geometry G2 (red line). Epsilon takes maximum value at the inlet to the gap, as it is shown in figure 4.19. For

geometry G1 this maximum is about $\varepsilon_{g1ke}^{\max} = 1.160 \cdot 10^6 m^2/s^3$, and for geometry G2 about $\varepsilon_{g2ke}^{\max} = 4.429 \cdot 10^5 m^2/s^3$. But, not far away from inlet to the gap, Epsilon for both geometries reaches similar value $\varepsilon = 2 \cdot 10^5 m^2/s^3$.

Epsilon averaged over the whole gap is $\varepsilon_{g1ke}^{avg} = 3.599 \cdot 10^5 m^2/s^3$ for geometry G1 and $\varepsilon_{g2ke}^{avg} = 2.011 \cdot 10^5 m^2/s^3$ for geometry G2.

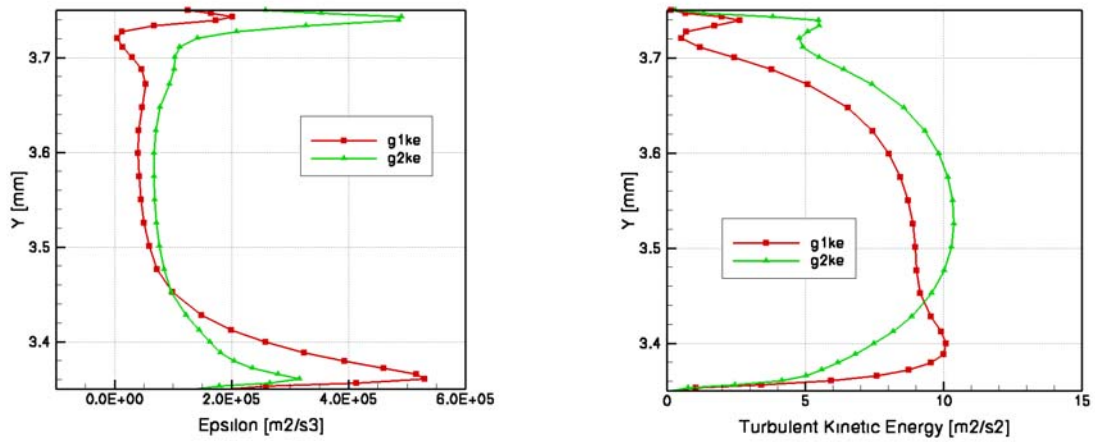

(a) (b)

Figure 4.20. Vertical profiles of the Epsilon (a) and Turbulent Kinetic Energy (b) in the middle of the gap for emulsifier with non-transparent (g1ke) and transparent (g2ke) processing element.

Figure 4.20 shows vertical profiles of the turbulent dissipation rate (Epsilon) and turbulent kinetic energy in the middle of the gap (Fig. 4.20) and 1mm behind processing element (Fig. 4.21). In all presented figures, differences between results obtained for geometry G1 (green points) and for geometry G2 (red points) are not too big.

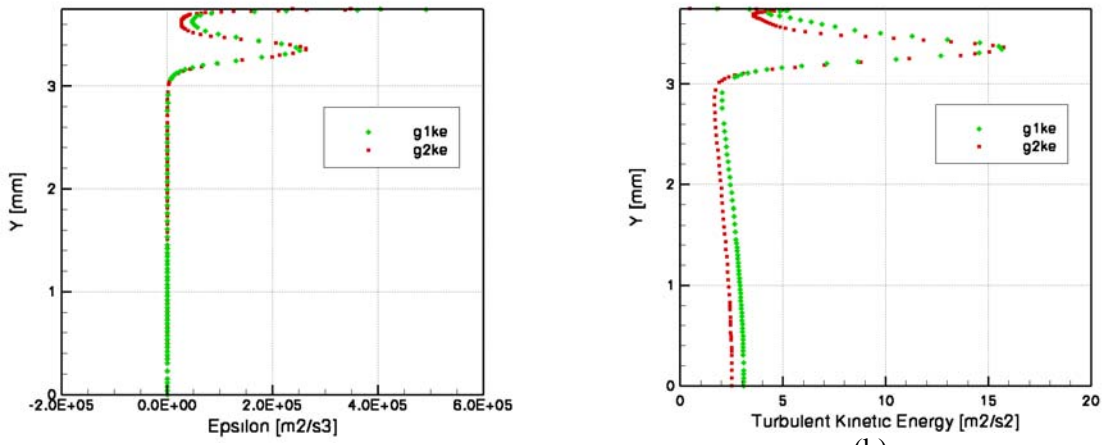

(a) (b)

Figure 4.21. Vertical profiles of the Epsilon (a) and Turbulent Kinetic Energy (b) 1mm after processing element for emulsifier with non-transparent (g1ke) and transparent (g2ke) processing element.

Figure 4.20a shows that in the gap Epsilon reaches maximum value in the vicinity of the walls of the gap, and turbulent kinetic energy – in the central region of the gap (Fig. 4.20b).

Figure 4.21a shows that Epsilon profile located 1mm behind processing element reaches high value in the vicinity of the wall. Then Epsilon decreases and reaches high value 0.5mm below wall, again, where occurs mixing of the fluid with high velocity value flowed from gap and fluid with low velocity value behind processing element.
Similar distribution is for turbulent kinetic energy (Fig. 4.21b), which reaches maximum value 0.5mm below wall, also.

4.5 Comparison of the experimental and numerical results

For verification of the numerical simulation, comparison of numerical and experimental results was done. Figure 4.22 shows profiles of the velocity x-component obtained from numerical simulation (green points) and from PIV measurements (red line) 1mm behind processing element (Fig. 4.22a), 3mm behind processing element (Fig. 4.22b), and 8mm behind processing element (Fig. 4.22c).

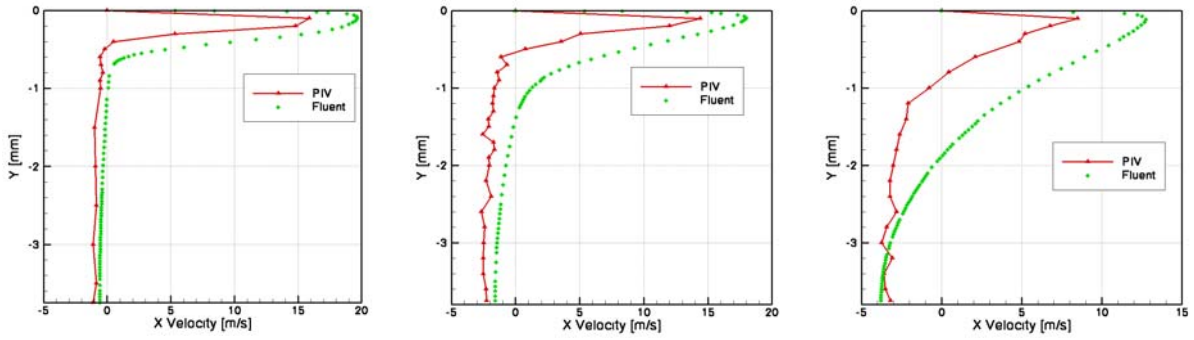

Figure 4.22. Comparison of numerical and experimental x-velocity vertical profiles for selected regions in emulsifier: 1mm after processing element (a), 3mm (b) and 8mm (c).

In the vicinity of the processing element, qualitative and quantitative conformity of the numerical and experimental results is fairly good (Fig. 4.22a,b). But in the profile located 8*mm* behind processing element (Fig. 4.22c) difference between numerical and experimental results is significant, but x-velocity profiles are similar, still.

4.6 Estimation of the maximum oil-drops size based on the numerical results

Based on numerical simulations results estimation of the obtained oil drops size in investigated emulsification process was done. Two different theories were used:

- Hinze theory:

$$d_{\max} = 0.749 \frac{\sigma^{3/5}}{\rho_c^{3/5} \cdot \varepsilon^{2/5}},$$

where: d_{max} – maximum oil droplets diameter, σ – interfacial tension, ρ_c – dispersing medium density, ε - turbulent dissipation rate;

- Davis theory

$$d_{\max} = \frac{K}{\rho_c^{3/5} \cdot \varepsilon^{2/5}} \left(\sigma + \frac{\mu_d \sqrt{2} (\varepsilon \cdot d_{\max})^{1/3}}{4} \right)^{3/5},$$

where: d_{max} – maximum oil droplets diameter, K – constant (K = 0.748), σ – interfacial tension, ρ_c – dispersing medium density, ε - turbulent dissipation rate, μ_d – dispersed medium viscosity.

Estimation was done for two silicone oils:

- silicone oil S50 with viscosity $\mu_d^{S50} = 50 mPas$,
- silicone oil S500 with viscosity $\mu_d^{S500} = 500 mPas$.

As dispersing medium was used substance with properties:

- density ρ_c=*998 kg/m*^{3},
- interfacial tension σ =*5.5 mN/m*

that corresponds to properties of de-ionised water with 1%wt anionic surfactant sodium dodecyl sulphate (SDS).

Figure 4.23 shows calculated dependence between oil droplets diameter and turbulent dissipation rate (Epsilon) for both silicone oils using Hinze and Davis theory. For small Epsilon value, small changes of the Epsilon strongly influence changes of the oil drops diameter. For Epsilon above $2 \cdot 10^5 m^2/s^3$, changes of the Epsilon insignificantly influence changes of the oil droplets diameter.

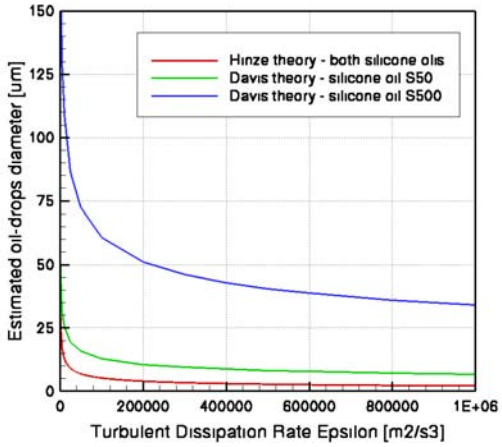

Figure 4.23. Estimated dependence between Turbulent Dissipation Rate *Epsilon* and oil-drops diameter for used silicone oils.

Table 4.4 collect results of estimation of the oil droplets diameter for:

- two geometries of emulsifier model used in numerical simulations: geometry G1 and G2,
- both used silicone oils: S50 and S500,
- Hizne theory and Davis theory,

- maximum value of turbulent dissipation rate ε_{max} in the gap and averaged over whole gap value of turbulent dissipation rate ε_{avg}.

Table 4.4. Results of the oil drops diameter estimation.

		Hinze theory both oils [μm]	Davis theory oil S50 [μm]	Davis theory oil S500 [μm]
Emulsifier with transparent processing element	max. epsilon value in gap $\varepsilon_{max}=4.429\cdot10^5$ m^2/s^3	2.89	8.44	41.77
	avg. epsilon value in gap $\varepsilon_{avg}=2.011\cdot10^5$ m^2/s^3	3.96	10.55	50.98
Emulsifier with non-transparent processing element	max. epsilon value in gap $\varepsilon_{max}=1.044\cdot10^6$ m^2/s^3	2.05	6.65	33.59
	avg. epsilon value in gap $\varepsilon_{avg}=3.453\cdot10^5$ m^2/s^3	3.19	9.05	44.47

4.7 Conclusions

Numerical modelling confirmed main details of the velocity flow field measured by the micro-PIV method. It gives confidence that generated numerical data can be applied for predicting conditions for droplets break-up in a shear flow. The laminar and turbulent flow models are successfully applied producing similar flow structure. It indicates that intensity of turbulence is relatively low and that the droplets break-up process may depend not only on the turbulent dissipation energy but mainly on the shear gradients of strongly fluctuating in time quasi-laminar flow field.

5. Publications list

[1] A. Słowicka, Z.A. Walenta, *Conditions for creating thin liquid layers a the contact surface of two other liquids*, Mechanics of the 21st Century, Proceedings of the 21st ICTAM with CD-ROM, Eds. W. Gutkowski, T.A. Kowalewski, Springer Verlag 2005

[2] J. Blawzdziewicz, E. Wajnryb, High-frequency linear viscosity of emulsions composed of two viscoelastic fluids, Mechanics of the 21st Century, Proceedings of the 21st ICTAM with CD-ROM, Eds. W. Gutkowski, T.A. Kowalewski, Springer Verlag 2005

[3] A. Słowicka, Z.A. Walenta, *Creating a thin liquid layer at the contact surface of two other liquids*, Abstract Book, Euromech Colloquium 472: "Microfluidics and Transfer", Grenoble 2005

[4] S. Błonski, T.A. Kowalewski, *Micro-flows investigations in production process of emulsions containing nanoparticles,* Abstract Book, Euromech Colloquium 472: "Microfluidics and Transfer", Grenoble 2005

6. Summary and conclusions

1. Velocity measurements (micro-PIV) indicate almost uniform velocity flow field in the gap region. It means that turbulence is still not fully developed and only strong shear gradients may be responsible for the droplet break-up. After processing element there is strong recalculation zone with a reversal flow. The turbulent fluctuations of the velocity field, break-up of the flow symmetry observed in this region indicate that here probably occurs transition from laminar to turbulent flow regime.
2. Visualisation of droplets break-up in the homogeniser indicates that the process takes place few millimetres behind processing element. We could not find "large" droplets in the gap and we do not observe droplets break-up process. However, there are "large" droplets observed behind the gap. It is not clear if these droplets are created due to the agglomeration in the dead-water region (re-circulation zone after the gap), or we were unable to record large droplets in the gap by our camera. The flow observations are performed in the vicinity of the channel centre only. It is possible that some large droplets are trapped by the sidewalls of the gap, not recorded by the camera. They may enter the re-circulation zone, and being transported by a cross-flow to the centre become visible in the field of observation. It would indicate existence of a strong cross-flow in this region, in fact partially visible in our velocity field measurements.
3. The capillary break-up of the liquid jet in co-flow is used to produce single droplets. Well-controlled production of single micro-droplets is necessary for studying accumulation of nano-particles at the interface, the main target of the project. The experiments performed indicated that small droplets (1μm) are created as satellites during fluid-threads break-up. The process of a micro-thread formation was previously observed and investigated [Kowalewski, Fluid Dyn. Res. 1996] for break-up of viscous jets in air. Similar process is found in the present study for two-liquids system. A hydrodynamic separation of small satellites created after the thread break-up is perhaps the simplest method of utilizing jet break-up for micro-droplets production.
4. Numerical modelling confirmed main details of the velocity flow field measured by the micro-PIV method. It gives confidence that generated numerical data can be applied for predicting conditions for droplets break-up in a shear flow. The laminar and turbulent flow models are successfully applied producing similar flow structure. It indicates that intensity of turbulence is relatively low and that the droplets break-up process may depend not only on the turbulent dissipation energy but mainly on the shear gradients of strongly fluctuating in time quasi-laminar flow field.